Polariton Spectra under the Collective Coupling Regime. I. Efficient Simulation of Linear Spectra and Quantum Dynamics

M. Elious Mondal,[1, a)] A. Nickolas Vamivakas,[2, 3] Steven T. Cundiff,[4] Todd D. Krauss,[1, 2] and Pengfei Huo[1, 2, b)]
[1)] *Department of Chemistry, University of Rochester, Rochester, New York, 14627, USA*
[2)] *The Institute of Optics, Hajim School of Engineering, University of Rochester, Rochester, NY 14627, USA*
[3)] *Department of Physics and Astronomy, University of Rochester, Rochester, NY 14627, USA*
[4)] *Department of Physics, University of Michigan, Ann Arbor, MI 48109, USA*

We outline two general theoretical techniques to simulate polariton quantum dynamics and optical spectra under the collective coupling regimes described by a Holestein-Tavis-Cummings (HTC) model Hamiltonian. The first one takes the advantage of sparsity of the HTC Hamiltonian, which allows one to reduce the cost of acting polariton Hamiltonian onto a state vector to the linear order of the number of states, instead of the quadratic order. The second one is applying the well-known Chebyshev series expansion approach for quantum dynamics propagation and applying them to simulate the polariton dynamics in the HTC system, allowing one to use a much larger time step for propagation and only requires a few recursive operations of the Polariton Hamiltonian acting on state vectors. These two theoretical approaches are general and can be applied to any trajectory-based non-adiabatic quantum dynamics methods. We apply these two techniques with our previously developed Lindblad-Partially Linearized Density Matrix ($\mathcal{L}$-PLDM) approach to simulating the linear absorption spectra of the HTC model system, with both inhomogeneous site energy disorder as well as dipolar orientational disorders. Our numerical results agree well with the previous analytic and numerical work.

I. INTRODUCTION

Coupling molecular excitations to a quantized radiation field inside an optical cavity produces a set of light-matter hybrid states known as polaritons. These polariton states, which are a hybridization of matter excitation and photonic excitation, have shown interesting photophysical properties. In particular, the light-matter interaction has been shown to effectively reduce the coupling between excitons and phonons, which is commonly referred to as the polaron decoupling effect.[1,2] This polaron decoupling effect results in an enhanced charge transfer rate constant,[1] reduction of the homogeneous linewidth of spectra,[3,4] and causes ballistic exciton-polariton transport.[5–7] In particular, the exciton-polariton coherence lifetime could be significantly prolonged due to reduced coupling with the phonon bath.[4,8]

Linear[9,10] and nonlinear spectroscopy[4,11–15] are powerful measurements that provide a fundamental understanding of the photophysics of polariton systems. To capture the essential features of polariton photophysics, one needs to simulate N molecules collectively coupled to the cavity mode, typically using the Holestein-Tavis-Cummings (HTC) model Hamiltonian. Further, one needs to explicitly incorporate exciton energy disorders (inhomogeneous disorder) and dipole orientational disorders for the molecule-cavity coupling interactions. In the typical experimental setup, one couple $N = 10^3 - 10^4$ Nanoplatelet to the cavity,[8,16–19] or at least $N = 10^6$ organic molecules to one cavity mode. When there is no disorder present in the HTC Hamiltonian, one can in principle take advantage of the permutational symmetry of the problem and solve the problem with a mean field solution[20,21] or the recently proposed CUT-E approach[22,23] for the zero-temperature case and with a single high-frequency vibration mode per molecule. With the presence of various disorders (and no apparent symmetry in the system), it is computationally challenging to directly stimulate the polariton dynamics when there are a large N of molecules coupled to the cavity, although there is progress in effectively describing static disorders as energy bins while taking advantage of the symmetry in HTC-type Hamiltonian.[22,23] The Tensor Train decomposition method[24] in principle could handle HTC-type dynamics with disorders, but remains computationally expensive due to the full quantum mechanical treatment for all degrees of freedom (DOFs).

In our previous work, we have combined the partial linearized density matrix (PLDM) approach[25–28] with stochastic Lindblad dynamics to simulate polaritonic spectroscopy in lossy cavities. To include the cavity loss dynamics, we develop stochastic Lindbald dynamics, which exactly reproduce the Lindblad dynamics when averaged over an ensemble of trajectories. With simulated linear and 2D Electronic Spectra (2DES) of the polariton, we systematically investigated the influence of the light-matter coupling strength and cavity loss rate on the optical signals. In particular, we demonstrate that the polariton coherence (interpreted from the off-diagonal peak of the 2D electronic spectra) can be significantly prolonged by increasing the light-matter coupling strength, providing a theoretical verification of the po-

---

[a)] Electronic mail: mmondal@ur.rochester.edu
[b)] Electronic mail: pengfei.huo@rochester.edu

laron decoupling effect.[4] We now aim to generalize our approach to the collective coupling situation, where a large N of molecules are collectively coupled to a cavity mode, with the presence of various types of molecular disorders.

In a series of two papers, we aim to develop an efficient and accurate approach to simulate the nonlinear spectra of the molecule-cavity hybrid system under the collective coupling regime. In Paper I (this work), we will focus on introducing two theoretical techniques that allow one to significantly reduce the computational cost of simulating the quantum dynamics of the HTC system with various types of disorders. We will focus on the linear spectra simulation. In Paper II, we will outline the theoretical details of stimulating 2DES for the polariton system under the collective coupling regime, with new computational techniques for focusing the algorithm of the PLDM simulation.

In this paper (paper I), we outline two general theoretical techniques. The first one is related to the sparsity of the HTC Hamiltonian, which allows one to reduce the cost for action of polariton Hamiltonian onto a state vector to the linear order in the number of states, instead of the quadratic order. The second one is applying the well-known Chebyshev series expansion approach for quantum dynamics propagation and applying them to simulate the polariton dynamics in the HTC system. The Chebyshev expansion allows us to use a much larger time step for propagation and only requires a few recursive operations of the Polariton Hamiltonian acting on state vectors, which can further take advantage of the first technique we developed in this work. These two theoretical approaches are general and can be applied to any trajectory-based non-adiabatic quantum dynamics methods[29–34] or gaussian wavepacket-based approaches.[35,36] We focus on simulating the linear absorption spectra of the HTC model system, with both inhomogeneous site-energy disorder as well as dipolar orientational disorders. With the significant reduction of the computational costs, we can directly simulate collective polariton dynamics with up to $N = 10^5$. Our numerical results agree well with the previous analytic[37] and numerical work.[38]

II. POLARITON QUANTUM DYNAMICS

A. Model Hamiltonian

We describe the system of N-molecules coupled to a single cavity mode by the Holestein-Tavis-Cummings[39] Hamiltonian

$$\hat{H}_{\mathrm{HTC}} = \hat{H}_{\mathrm{s}} + \hat{H}_{\mathrm{b}} + \hat{H}_{\mathrm{sb}}, \tag{1}$$

where $\hat{H}_{\mathrm{s}}$ is the Hamiltonian of the system, $\hat{H}_{\mathrm{b}}$ is the Hamiltonian for bath DOF and $\hat{H}_{\mathrm{sb}}$ is the system-bath interaction. The system Hamiltonian consists of excitonic and photonic DOF,

$$\hat{H}_{\mathrm{s}} = \left(\hat{H}_{\mathrm{ex}} + \hat{H}_{\mathrm{ph}}\right) \otimes \hat{\mathbb{1}}_{\mathrm{b}} + \hat{H}_{\mathrm{ex-ph}} \otimes \hat{\mathbb{1}}_{\mathrm{b}}, \tag{2}$$

where $\hat{H}_{\mathrm{ex}}$ is the molecular (excitonic) Hamiltonian, $\hat{H}_{\mathrm{ph}}$ is the photonic Hamiltonian, $\hat{H}_{\mathrm{ex-ph}}$ is the exciton-photon interaction and $\hat{\mathbb{1}}_{\mathrm{b}}$ is the identity operator in the bath subspace. The excitonic Hamiltonian consists of N uncoupled molecules, each with an onsite energy ε_n. The excitonic hamiltonian can be written as

$$\hat{H}_{\mathrm{ex}} = \sum_{n}^{N} \varepsilon_n \hat{\sigma}_n^{\dagger} \hat{\sigma}_n \otimes \hat{\mathbb{1}}_{\mathrm{ph}} \tag{3}$$

Here, $\hat{\sigma}_n^{\dagger} = |e_n\rangle\langle g_n|$ and $\hat{\sigma}_n = |g_n\rangle\langle e_n|$ creates annilates an excitation on the n_{th} molecule, respectively, with $|g_n\rangle$ and —$e_n\rangle$ as the ground and excited states for molecule n, and $\hat{\mathbb{1}}_{\mathrm{ph}}$ is the identity operator for the photonic subspace. The photonic Hamiltonian is described by a single cavity mode

$$\hat{H}_{\mathrm{ph}} = \hat{\mathbb{1}}_{\mathrm{ex}} \otimes \hbar\omega_{\mathrm{c}} \left(\hat{a}^{\dagger}\hat{a} + \frac{1}{2}\right) \tag{4}$$

where $\hat{a}^{\dagger}$ and $\hat{a}$ create and annihilate a photonic excitation (a photon) associated with the cavity mode, respectively, with energy $\hbar\omega_{\mathrm{c}}$ and $\hat{\mathbb{1}}_{\mathrm{ex}}$ is the identity operator for the excitonic subspace. The operators obey the commutation relation $[\hat{a}, \hat{a}^{\dagger}] = \hat{\mathbb{1}}_{\mathrm{ph}}$. We further assume the rotating wave approximation for the light-matter coupling term

$$\hat{H}_{\mathrm{ex-ph}} = \sum_{n} \hbar g_{\mathrm{c}}^{n} \left(\hat{\sigma}_n^{\dagger}\hat{a} + \hat{\sigma}_n \hat{a}^{\dagger}\right), \tag{5}$$

with g_{c}^{n} being the coupling strength for the n_{th} exciton,

$$g_{\mathrm{c}}^{n} = \sqrt{\frac{\hbar\omega_{\mathrm{c}}}{2\mathcal{V}\epsilon_{\mathrm{c}}}}\hat{\boldsymbol{\mu}}_n \cdot \hat{\mathbf{e}} = \sqrt{\frac{\hbar\omega_{\mathrm{c}}}{2\mathcal{V}\epsilon_{\mathrm{c}}}}\mu_n \cdot \cos\theta_n. \tag{6}$$

Here, μ_n is the magnitude of the transition dipole moment of the n_{th} exciton, $\hat{\mathbf{e}}$ is the filed polarization direction, θ_n is the angle between $\hat{\boldsymbol{\mu}}_n$ and $\hat{\mathbf{e}}$. Further, $\mathcal{V}$ is the mode volume of the cavity, and ϵ_{c} is the permittivity inside the cavity.

In addition, each molecular exciton is also coupled to a number of phonon modes that constitute the molecular bath. The bath Hamiltonian is described by

$$\hat{H}_{\mathrm{b}} = \hat{\mathbb{1}}_{\mathrm{s}} \otimes \left[\frac{1}{2}\sum_{n=1}^{N}\sum_{\nu}\left(\hat{P}_{n,\nu}^{2} + \omega_{n,\nu}^{2}\hat{R}_{n,\nu}^{2}\right)\right] \tag{7}$$

where $\hat{P}_{n,\nu}$ and $\hat{R}_{n,\nu}$ are the momentum and position operator of the ν_{th} phonon on n_{th} matter site of frequency $\omega_{n,\nu}$, and $\hat{\mathbb{1}}_{\mathrm{s}} = \hat{\mathbb{1}}_{\mathrm{ex}} \otimes \hat{\mathbb{1}}_{\mathrm{ph}}$ is the identity operator of the "system" subspace that includes the excitonic and photonic DOF. These bath DOF are coupled bi-linearly to the excitonic sites providing diagonal fluctuations to on-site energies

$$\hat{H}_{\mathrm{sb}} = \sum_{n} \left(\hat{\sigma}_n^{\dagger}\hat{\sigma}_n \otimes \hat{\mathbb{1}}_{\mathrm{ph}}\right) \otimes \left(\sum_{\nu} C_{n,\nu}\hat{R}_{n,\nu}\right) \tag{8}$$

where $C_{n,\nu}$ is the strength of coupling between n_{th} exciton and ν_{th} phonon (vibratrional mode). For the n_{th} exciton, the phonon frequencies and coupling strength are sampled from the Debye spectral density[40]

$$J_n(\omega) = \frac{\pi}{2}\sum_{\nu}\frac{C_{n,\nu}^2}{\omega_{n,\nu}}\delta(\omega-\omega_{n,\nu}) = \frac{2\lambda_{\mathrm{b}}\omega_{\mathrm{b}}\omega}{\omega_{\mathrm{b}}^2+\omega^2}, \tag{9}$$

with λ_{b} being the bath reorganisation energy and ω_{b} being the characteristic frequency of the bath. To perform linear and non-linear spectroscopy simulation, we use the matter dipole operator for computing multi-time correlation functions[41–45]

$$\hat{\mu} = \sum_{n}^{N} \mu_n \left(\hat{\sigma}_n^{\dagger} + \hat{\sigma}_n\right) \otimes \hat{\mathbb{1}}_{\mathrm{ph}} \tag{10}$$

where μ_n is the magnitude of the transition dipole of excitation for n^{th} molecule. Cavity loss is not explicitly considered in the Hamiltonian. The loss effect is incorporated through the stochastic Lindblad approach developed in our previous work,[46,47] with a brief summary provided in the Appendix A.

B. Polariton States

The diabatic eigenstates of $\hat{H}_{\mathrm{s}}$ are defined as

$$\hat{H}_{\mathrm{s}}|\alpha\rangle = \epsilon_{\alpha}|\alpha\rangle. \tag{11}$$

When only considering the single excitation subspace $|j\rangle = \{|g\rangle \otimes |1\rangle, |e_n\rangle \otimes |0\rangle\}$ (where $|g\rangle \equiv \otimes|g_n\rangle$) with degenerate exciton energy $\varepsilon_n = \varepsilon$, and identical light-matter couplings $g_{\mathrm{c}}^n = g_{\mathrm{c}}$, Eq. 11 has well known analytic solution, with two bright polariton states[10,48–51]

$$|+\rangle = \cos\Theta_N \left[\frac{1}{\sqrt{N}}\sum_{n=1}^{N}|e_n\rangle \otimes |0\rangle\right] + \sin\Theta_N|g\rangle \otimes |1\rangle, \tag{12a}$$

$$|-\rangle = -\sin\Theta_N \left[\frac{1}{\sqrt{N}}\sum_{n=1}^{N}|e_n\rangle \otimes |0\rangle\right] + \cos\Theta_N|g\rangle \otimes |1\rangle, \tag{12b}$$

where the mixing angle is

$$\Theta_N = \frac{1}{2}\tan^{-1}\left[\frac{2\sqrt{N}\hbar g_{\mathrm{c}}}{\hbar\omega_{\mathrm{c}}-\varepsilon}\right] \in [0, \frac{\pi}{2}), \tag{13}$$

and $N-1$ dark states for $k \in \{1, \cdots, N-1\}$

$$|\mathrm{D}_k\rangle = \frac{1}{\sqrt{N}}\sum_{n=1}^{N}\exp\left(-2\pi i\frac{nk}{N}\right)|e_n\rangle \otimes |0\rangle, \tag{14}$$

The polariton states and dark states have the energy of

$$\varepsilon_{\pm} = \frac{\varepsilon+\hbar\omega_{\mathrm{c}}}{2} \pm \frac{1}{2}\sqrt{(\varepsilon-\hbar\omega_{\mathrm{c}})^2+4N\hbar^2 g_{\mathrm{c}}^2}, \tag{15a}$$

$$\varepsilon_{\mathrm{D}_k} = \varepsilon. \tag{15b}$$

where the eigenenergies of polariton states are split from the original exciton energy and the Dark states have degenerate energies that are identical to the exciton energy. As shown in Ref. 49, the analytic solution[10,48,49] is also available for $\hat{H}_{\mathrm{s}}$. For the zero-detuning case $\varepsilon = \hbar\omega_{\mathrm{c}}$, the Rabi splitting is $\hbar\Omega_{\mathrm{R}} = \varepsilon_+ - \varepsilon_- = 2\sqrt{N}\hbar g_{\mathrm{c}}$, and the strong coupling limit[39,50] is achieved when $\Omega_{\mathrm{R}} \gg \frac{1}{2}(\Gamma+\kappa)$, where Ω_{R} is the cavity loss rate (linewidth of the cavity transmission spectra, $\tau_{\mathrm{c}} = 1/\Gamma$ is the cavity lifetime) and κ is the exciton linewidth.

C. Trajectory Based Quantum Dynamics Approach

In this work, we consider the trajectory-based quantum dynamics simulations for the HTC model, which treat $\hat{H}_{\mathrm{s}} + \hat{H}_{\mathrm{sb}}$ as the quantum subsystem,

$$\hat{H}_{\mathrm{Q}} = \hat{H}_{\mathrm{s}} + \hat{H}_{\mathrm{sb}}, \tag{16}$$

and $\hat{H}_{\mathrm{b}}$ as the classical subsystem. We want to explicitly consider the static energy disorders in site energy ε_n (inhomogeneous disorder, see Eq. 74) as well as the dipole orientation disorder in $\cos\theta_n$ for the light-matter interaction terms.

In particular, we will use the partial linearized density matrix (PLDM) dynamics method,[25–27,47,52,53] but the outlined theoretical schemes can be applied to any mixed quantum-classical (MQC) method, including the mean-field Ehrenfest dynamics, the trajectory surface hopping approach[54,55], or trajectory-based semiclassical methods such as the linearized semiclassical approach[56–59] and symmetrical quasiclassical approach (SQC)[60,61].

These trajectory-based quantum dynamics methods typically require the quantum propagation of the quantum state vector

$$i\hbar\frac{\partial}{\partial t}|\Psi(t)\rangle = \hat{H}_{\mathrm{Q}}(\mathbf{R}(t))\,|\Psi(t)\rangle\,. \tag{17}$$

For a given diabatic basis $\{|j\rangle\}$ (for example, Eq. 22-Eq. 24), one can expand $|\psi(t)\rangle = \sum_j c_j(t)|j\rangle$, and Eq. 17 becomes

$$i\hbar\dot{c}_k(t) = \sum_{k}\langle k|\hat{H}_{\mathrm{Q}}(\mathbf{R}(t))|j\rangle \cdot c_j(t). \tag{18}$$

Note that both $\hat{H}_{\mathrm{Q}}$ and $|\Psi(\mathbf{R}(t))\rangle$ depend parametrically on the bath configuration, $\mathbf{R}(t) \equiv \{R_{n,\nu}(t)\}$. The nuclear DOF is updated through the classical equations of motion, with different types of forces that depend on $\nabla_{\mathbf{R}}(\hat{H}_{\mathrm{sb}} + \hat{H}_{\mathrm{b}})$, such as Ehrenfest dynamics (and similarly for other mean-field-like approaches) with $\mathcal{F} =$

$-\sum_{jk} c_j^* c_k \nabla_{\mathbf{R}} \langle j|(\hat{H}_{\mathrm{sb}}+\hat{H}_{\mathrm{b}})|k\rangle$, and for the HTC Hamiltonian special case, the nuclear force is

$$\mathcal{F} = -\sum_j |c_j|^2 \nabla_{\mathbf{R}} \langle j|(\hat{H}_{\mathrm{sb}}+\hat{H}_{\mathrm{b}})|j\rangle, \tag{19}$$

which is purely diagonal due to the diagonal $\hat{H}_{\mathrm{sb}}$ in the diabatic basis (Eq. 22-Eq. 24). For the trajectory surface hopping approach, the nuclear force is $\mathcal{F} = -\nabla_{\mathbf{R}} \langle J(\mathbf{R})|(\hat{H}_{\mathrm{sb}}+\hat{H}_{\mathrm{b}})|J(\mathbf{R})\rangle$, where $|J(\mathbf{R})\rangle$ is an active adiabatic surface (an eigenstate of $\hat{H}_{\mathrm{Q}}$) that is determined stochastically through a given algorithm (such as the most widely used fewest switches algorithm[54,55]).

The main challenge of solving Eq. 18 for the HTC Hamiltonian under the collective coupling regime is the large number of N that one has to incorporate. The right-hand side of the differential equation, $\hat{H}_{\mathrm{Q}}|\Psi\rangle$, requires the operation of $\hat{H}_{\mathrm{Q}}$ matrix on a state vector $c_j(t)$. For the HTC Hamiltonian with N molecules and one cavity mode, there are $\mathcal{K} = N+1 \propto \mathcal{O}(N)$ states in the single excitation subspace and $\mathcal{K} = N(N-1)/2+N+1 \propto \mathcal{O}(N^2)$ states in the double excitation subspace. The force evaluation for a mean-field-like approach of the HTC model (Eq. 19), on the other hand, only scales with $\mathcal{O}(\mathcal{K})$ due to the purely diagonal structure of $\hat{H}_{\mathrm{sb}}$, in the diabatic site basis. The typical experimental condition requires $N = 10^6 - 10^{12}$, resulting in a very large $\mathcal{K}$, and the computational work[12,24,29,30,38] is often limited by $N = 10^1 - 10^2$ due to the computational cost.

The other possibility is to consider the propagator approach instead of solving the TDSE (Eq. 18) directly. Note that $\hat{H}_{\mathrm{Q}}$ contains a static part of $\hat{H}_{\mathrm{s}}$ (with a very special symmetry) and a purely diagonal part $\hat{H}_{\mathrm{sb}}$ that depends on $\mathbf{R}(t)$. One can consider the following symmetrical Trotter splitting

$$|\Psi(t+\Delta t)\rangle \approx e^{-\frac{i}{\hbar}\hat{H}_{\mathrm{sb}}\Delta t/2} e^{-\frac{i}{\hbar}\hat{H}_{\mathrm{s}}\Delta t} e^{-\frac{i}{\hbar}\hat{H}_{\mathrm{sb}}\Delta t/2} |\Psi(t)\rangle\,, \tag{20}$$

with the accuracy up to $\mathcal{O}(\Delta t^3)$. Using a diabatic basis $|j\rangle$ and the polariton basis $|\alpha\rangle$ (see Eq. 11), one can rewrite Eq. 20 as

$$|\Psi(t+\Delta t)\rangle = \sum_k c_k(t+\Delta t)|k\rangle \tag{21}$$
$$\approx \sum_k |k\rangle \sum_{j\alpha} e^{-\frac{i}{\hbar}\lambda_k \Delta t/2} \langle k|\alpha\rangle e^{-\frac{i}{\hbar}\epsilon_\alpha \Delta t} \langle \alpha|j\rangle e^{-\frac{i}{\hbar}\lambda_j \Delta t/2} c_j(t),$$

where ϵ_α is the diabatic polariton energy defined in Eq. 11, $\lambda_j = \langle j|\hat{H}_{\mathrm{sb}}(\mathbf{R})|j\rangle$ is the pure diagonal contribution of the system-bath coupling (that parametrically depends on $\mathbf{R}$), and $c_j(t) = \langle j|\Psi(t)\rangle$. In principle, one needs to diagonalize $\hat{H}_{\mathrm{s}}$ to obtain ϵ_α and $\{\langle\alpha|j\rangle\}$ at a cost of $\mathcal{O}(\mathcal{K}^2)$ (see Ref. 62–64, due to the symmetry of $\hat{H}_{\mathrm{s}}$, instead of the usual cost of $\mathcal{O}(\mathcal{K}^3)$ for diagonalizing an arbitrary $\mathcal{K}\times\mathcal{K}$ matrix). Nevertheless, because these are diabatic quantities, one can in principle compute them only once and store them. Of course, when only single- and double-excitation subspaces are considered, these results are (almost) analytically available.[10,48,49] When only considering the single excitation subspace $|j\rangle = \{|g\rangle\otimes|1\rangle, |e_n\rangle\otimes|0\rangle\}$, the expression of $\mathcal{S}_{kj}(\Delta t) \equiv \sum_\alpha \langle k|\alpha\rangle e^{-\frac{i}{\hbar}\epsilon_\alpha \Delta t}\langle\alpha|j\rangle$ is analytically available and can be precomputed and stored. One just needs to multiply the $\tilde{S}_{kj} \equiv e^{-\frac{i}{\hbar}\lambda_k \Delta t/2}\mathcal{S}_{kj}(\Delta t) e^{-\frac{i}{\hbar}\lambda_j \Delta t/2}$ matrix onto the $c_j(t)$ column matrix to get the result of $c_k(t+\Delta t)$, which in principle still requires a cost of $\mathcal{O}(N^2)$.

As such, for the quantum dynamics problem of the HTC system, the main computational bottleneck is the $\hat{H}_{\mathrm{Q}}|\Psi\rangle$ evaluation. One would also want to avoid directly diagonalizing $\hat{H}_{\mathrm{Q}}$, as well as increase the time step Δt for the dynamics propagation as much as possible (because each step requires at least one $\hat{H}_{\mathrm{Q}}|\Psi\rangle$ evaluation) while keeping the propagation stable. In the following sections, we introduce several techniques that can significantly reduce the computational costs of propagating Eq. 17. These techniques can be broadly applied to any MQC trajectory-based methods for polariton quantum dynamics simulations.

III. THEORETICAL APPROACHES

We demonstrate strategies to efficiently manipulate matrix-vector multiplications to reduce the computation cost of semiclassical simulations. When considering the single excitation subspace, the size of the Hilbert space $\mathcal{K} \propto \mathcal{O}(N)$, and solving the TDSE in principle requires operation of $\mathcal{O}(\mathcal{K}^2) \propto \mathcal{O}(N^2)$. When considering the Hilbert space up to the second excitation subspace (for 2DES simulations in paper II) $\mathcal{K} \propto \mathcal{O}(N^2)$, and the quantum dynamics simulation will in principle require a cost of $\mathcal{O}(\mathcal{K}^2) \propto \mathcal{O}(N^4)$. To reduce the scaling of the cost, we first demonstrate how the action of the $\hat{H}_{\mathrm{Q}}$ on $|\Psi(t)\rangle$ can be written as the sum of a simple Hadamard product of vectors that reduces matrix-vector multiplication from $\mathcal{O}(N^2)$ to $\mathcal{O}(N)$ for single excitation subspace and $\mathcal{O}(N^4)$ to $\mathcal{O}(N^2)$ for up to double excitation subspace. We demonstrate a similar scaling reduction for the action of the dipole operator on the wavefunction, which is relevant for linear and non-linear spectra calculations. We further apply a Chebyshev series expansion approach to simulate the polariton dynamics in the HTC system. The Chebyshev expansion allows us to use a much larger time step for propagation and only requires a few recursive operations of the Polariton Hamiltonian acting on state vectors, which can further take advantage of the scaling reduction due to the sparsity of the HTC Hamiltonian.

The theoretical approach we outlined here can be widely applicable to any mixed quantum-classical methods to simulate polariton dynamics (population, coherence, different types of correlation functions). The scaling reduction in the single excitation subspace is the most relevant part of the linear spectra simulation in this paper, whereas the scaling reduction in the double excitation subspace will be relevant for 2DES simulations in Paper II.

A. Efficient Evaluation of $\hat{H}_{\mathrm{Q}}\left|\Psi\right\rangle$ in the Double Excitation Subspace

The Quantum Dynamics propagation requires basic operator action of $\hat{H}_{\mathrm{Q}}\left|\Psi\right\rangle$ operation (see Eq. 17 and Eq. 18) using for example, RK4 method, or $\hat{O}\left|\Psi\right\rangle$ (see Eq. 36) in the Chebyshev expansion scheme (Eq. 35). For a $\mathcal{K}$-dimensional system in $\hat{H}_{\mathrm{Q}}$, this would in principle require $\mathcal{K}^2$ operations in matrix multiplications. However, we notice that the matrix of $\hat{H}_{\mathrm{Q}}$ in the HTC Hamiltonian is extremely sparse in the single and double excitation subspaces, which are the relevant subspaces for photophysics and spectroscopy measurements. Here, we take advantage of this sparsity to significantly reduce the scaling of the computational costs of quantum dynamics propagation.

We take the bare excitonic states and the photonic Fock states to form the diabatic basis. The collective ground state can be written as

$$\left|\mathrm{G}^0\right\rangle = \left(\bigotimes_n \left|g_n\right\rangle\right) \otimes \left|0\right\rangle . \tag{22}$$

Within the single excitation manifold, we can describe two kinds of diabatic states characterized by either purely matter or purely photonic excitation character

$$\left|\mathrm{E}^0_n\right\rangle = \left(\bigotimes_{m\neq n} \left|g_m\right\rangle\right) \otimes \left|e_m\right\rangle \otimes \left|0\right\rangle , \tag{23a}$$

$$\left|\mathrm{G}^1\right\rangle = \left(\bigotimes_n \left|g_n\right\rangle\right) \otimes \left|1\right\rangle . \tag{23b}$$

In the second excitation manifold, we get three additional types of states, with either double matter excitations, double photon excitation, or a mixed matter-photon excited state, expressed as follows

$$\left|\mathrm{E}^0_{nm}\right\rangle = \left(\bigotimes_{p\neq n,m} \left|g_p\right\rangle\right) \otimes \left|e_n\right\rangle \otimes \left|e_m\right\rangle \otimes \left|0\right\rangle , \tag{24a}$$

$$\left|\mathrm{E}^1_n\right\rangle = \left(\bigotimes_{n\neq m} \left|g_m\right\rangle\right) \otimes \left|e_n\right\rangle \otimes \left|1\right\rangle , \tag{24b}$$

$$\left|\mathrm{G}^2\right\rangle = \left(\bigotimes_n \left|g_n\right\rangle\right) \otimes \left|2\right\rangle . \tag{24c}$$

With the above basis, a general quantum state can be expanded in this double-excitation subspace as

$$\begin{aligned} \left|\Psi\right\rangle =& c_{\mathrm{G}^0}\left|\mathrm{G}^0\right\rangle + \sum_n c_{\mathrm{E}^0_n}\left|\mathrm{E}^0_n\right\rangle + c_{\mathrm{G}^1}\left|\mathrm{G}^1\right\rangle \\ &+ \sum_{n,m>n} c_{\mathrm{E}^0_{nm}}\left|\mathrm{E}^0_{nm}\right\rangle + \sum_n c_{\mathrm{E}^1_n}\left|\mathrm{E}^1_n\right\rangle + c_{\mathrm{G}^2}\left|\mathrm{G}^2\right\rangle \end{aligned} \tag{25}$$

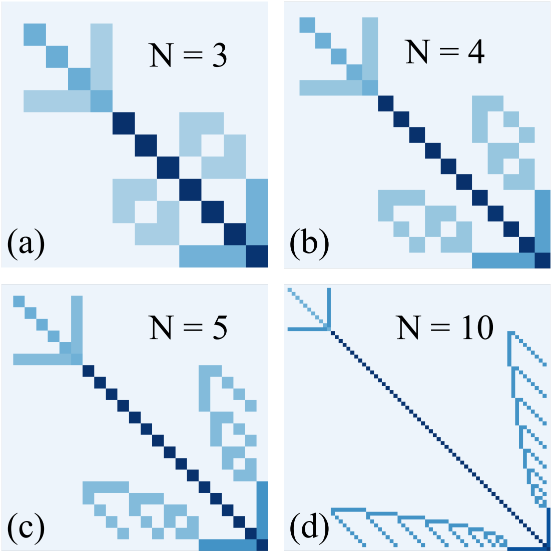

FIG. 1. The HTC Hamiltonian structure for N molecules. The light cyan color represents the zero matrix elements, whereas the darker blue represents the non-zero matrix elements. The order of the basis is the same as indicated in Eq. 25: from left to right for the row, and from top to bottom for the column. Panels (a)-(d) represent the Hamiltonian for $N = 3, 4, 5$, and 10 molecules, respectively, within the double excitation subspace.

where $c_j = \langle j|\Psi\rangle$. From now on, we will follow the order of the basis set expansion outlined in Eq. 25, and represent $\left|\Psi\right\rangle$ as

$$\left|\Psi\right\rangle \rightarrow \begin{bmatrix} c_{\mathrm{G}^0} \\ c_{\mathrm{E}^0_n} \\ c_{\mathrm{G}^1} \\ c_{\mathrm{E}^0_{nm}} \\ c_{\mathrm{E}^1_n} \\ c_{\mathrm{G}^2} \end{bmatrix} \tag{26}$$

The quantum Hamiltonian $\hat{H}_{\mathrm{Q}}$ in Eq. 50, when represented in the double excited diabatic basis, is very sparse in nature. Although the size of the Hamiltonian increases as $\mathcal{O}(N^4)$ for N molecules, the sparsity of the Hamiltonian (defined as the ratio between the number of nonzero matrix elements and the total number of matrix elements) scales as $1 - 1/N^2$ and very quickly converges to 1.

Fig. 1 demonstrates the increase in sparsity as N increases, with the nonzero matrix elements explicitly shown in a darker blue color, and with the basis order explicitly following Eq. 25. We can precompute the action of the sparse Hamiltonian, Eq. (50), on a general system quantum state in Eq. (25),

$$
\begin{aligned}
\hat{H}_{\mathrm{Q}}\,|\Psi\rangle &= \sum_{n}(c_{\mathrm{E}^0_n}\cdot\epsilon_n + \hbar g^n_{\mathrm{c}} c_{\mathrm{G}^1})|\mathrm{E}^0_n\rangle \qquad (27)\\
&+ \big(\hbar\omega_{\mathrm{c}}\cdot c_{\mathrm{G}^1} + \sum_{n} g^n_{\mathrm{c}} c_{\mathrm{E}^0_n}\big)|\mathrm{G}^1\rangle\\
&+ \sum_{n,m>n}\big[(\epsilon_n+\epsilon_m)\cdot c_{\mathrm{E}^0_{nm}} + \hbar(g^n_{\mathrm{c}} c_{\mathrm{E}^0_n} + g^m_{\mathrm{c}} c_{\mathrm{E}^0_m})\big]\,|\mathrm{E}^0_{nm}\rangle\\
&+ \sum_{n}\Big\{\sum_{m>n}\hbar g^m_{\mathrm{c}} c_{\mathrm{E}^0_{nm}} + (\epsilon_n+\hbar\omega_{\mathrm{c}})\cdot c_{\mathrm{E}^1_n} + \sqrt{2}\hbar g^n_{\mathrm{c}} c_{\mathrm{G}^2}\Big\}|\mathrm{E}^1_n\rangle\\
&+ \Big(2\hbar\omega_{\mathrm{c}}\cdot c_{\mathrm{G}^2} + \sqrt{2}\hbar\sum_{n} g^n_{\mathrm{c}} c_{\mathrm{E}^1_n}\Big)|\mathrm{G}^2\rangle,
\end{aligned}
$$

where

$$\epsilon_n = \varepsilon_n + \sum_{\nu} C_{n,\nu} R_{n,\nu}$$

is the exciton energy ε_n plus the bath fluctuation, with the instantaneous value of the bath coordinate $R_{n,\nu}$ (that is fixed during the Δt propagation). The above expansion in Eq. 27 can be expressed as the following Hadmmard product

$$\hat{H}_{\mathrm{Q}}\,|\Psi\rangle = \underbrace{|\epsilon_\Psi\rangle\odot|\Psi\rangle}_{\text{diagonal}} + \underbrace{\hbar g_{\mathrm{c}}\,|\Phi\rangle}_{\text{off}-\text{diagonal}}\ , \qquad (28)$$

which is the *first key result* of this work. In Eq. 28, the diagonal energies are accounted for by the vector

$$|\epsilon_\Psi\rangle \rightarrow \begin{bmatrix} 0\\ \epsilon_{\mathrm{E}^0_n}\\ \hbar\omega_{\mathrm{c}}\\ \epsilon_{\mathrm{E}^0_{nm}}\\ \epsilon_{\mathrm{E}^1_n}\\ 2\hbar\omega_{\mathrm{c}} \end{bmatrix}, \qquad (29)$$

Here, $\epsilon_{\mathrm{E}^0_n} = [\epsilon_1, \epsilon_2, ...\epsilon_N]^{\mathrm{T}}$ is the vector of exciton energies, $\epsilon_{\mathrm{E}^0_n} = [\epsilon_{12}, \epsilon_{13}, ...\epsilon_{(N-1)N}]^{\mathrm{T}}$ is the vector of double exciton energies and $\epsilon_{\mathrm{E}^1_n} = [\epsilon_1+\omega_{\mathrm{c}}, \epsilon_2+\omega_{\mathrm{c}}, ...\epsilon_N+\omega_{\mathrm{c}}]^{\mathrm{T}}$ is the vector of collective matter and photon excited state energies.

Further, the off-diagonal action of $\hat{H}_{\mathrm{Q}}$ on $|\Psi\rangle$ is accounted by the vector

$$|\Phi\rangle \rightarrow \begin{bmatrix} 0\\ c_{\mathrm{G}^1}\cdot\mu_n\mathrm{cos}\theta_n\\ \sum_n c_{\mathrm{E}^0_n}\cdot\mu_n\mathrm{cos}\theta_n\\ c_{\mathrm{E}^1_n}\cdot\mu_n\mathrm{cos}\theta_n + c_{\mathrm{E}^1_m}\cdot\mu_m\mathrm{cos}\theta_m\\ \sum_{m>n} c_{\mathrm{E}^0_{nm}}\cdot\mu_m\mathrm{cos}\theta_m + \sqrt{2}c_{\mathrm{G}^2}\cdot\mu_n\mathrm{cos}\theta_n\\ \sqrt{2}\sum_n c_{\mathrm{E}^1_n}\cdot\mu_n\mathrm{cos}\theta_n \end{bmatrix}, \qquad (30)$$

and when there is no dipole orientation disorders, simply set $\cos\theta_n = 1$ in the above expression.

The operation in Eq. 28 has a *linear* scaling in the number of states $\mathcal{O}(\mathcal{K})$, and thus $\propto \mathcal{O}(N)$ for a single excitation space and $\propto \mathcal{O}(N^2)$ double excitation space when having N-molecules for the polaritonic systems. The action of $\hat{H}_{\mathrm{Q}}$ on $|\Psi\rangle$ as outlined in Eq. 28 can be used to accurately calculate electronic evolution via a simple RK4 solution of Eq. 17 or through polynomial expansions of exponential propagators such as the Chebyshev series, which will be discussed next.

B. Chebyshev Series Expansion for Quantum Dynamics Propagation

To solve TDSE in Eq. 17, one can use many numerical methods, such as the RK4 solution of Eq. 17 or using the symplectic integrator.[65] These approaches can still take advantage of the sparsity properties of the Hamiltonian outlined in Sec. III A. The numerical challenges for these propagation-based methods are the requirement of relatively small Δt for stable propagation. Due to the large N considered in the HTC Hamiltonian, each propagation step remains computationally expensive.

To use a relatively large Δt, we use the Chebyshev polynomial expansion[66] approach to solve the TDSE. During a time Δt where the nuclear configuration $\mathbf{R}$ is fixed, the propagation can be expressed as

$$|\Psi(t+\Delta t)\rangle = \hat{U}(\Delta t)\,|\Psi(t)\rangle = \exp\left(-\frac{i}{\hbar}\hat{H}_{\mathrm{Q}}\Delta t\right)|\Psi(t)\rangle \qquad (31)$$

where the Chebyshev expansion of the evolution operator is expressed[66] as

$$\hat{U}(\Delta t)\,|\Psi\rangle = b_0(z)|\Psi^{(0)}\rangle + \sum_{n=1}^{\infty}\phi_n(z)b_n(z)|\Psi^{(n)}\rangle \qquad (32)$$

where $|\Psi^{(0)}\rangle = |\Psi(t)\rangle$, and $\{b_n\}$ are the bessel-function coefficients of the first type. The number of coefficients required for the above expansion is dictated by the (energy-time) uncertainty parameter

$$z = \frac{\delta_E\cdot\Delta t}{2\hbar}, \qquad (33)$$

where δ_E is the spectral radius (the energy difference between the highest and the lowest eigenenergy for $\hat{H}_{\mathrm{Q}}$). For $z \leq 1$, one only needs to include the first few terms of the expansion. In the Chebyshev expansion approach, a large time step Δt or a higher spectral radius δ_E results in a higher z value which necessitates the requirement of more number of terms in the expansion, Eq. 32.

Further, $\phi_n(z)$ in Eq. 32 is a phase factor that contains information on the shift in the energy axis due to the normalization of the Hamiltonian, given by

$$\phi_n(z) = 2i^n\mathrm{exp}\left(\frac{i}{\hbar}\left[\frac{\delta_E}{2}+\epsilon_{\mathrm{min}}\right]\Delta t\right). \qquad (34)$$

Here, δ_E corresponds to the approximate spectral radius of $\hat{H}_{\mathrm{Q}}$ and ϵ_{min} is an estimate of the lowest eigenvalue of $\hat{H}_{\mathrm{Q}}$. For the Chebyshev method, one only needs a rough estimate for δ_E and ϵ_{min}, which requires a rough estimation of the lowest and highest eigenvalues of $\hat{H}_{\mathrm{Q}}$.

The n_{th} order term of the Chebyshev expansion in Eq. 32 is calculated by the recursion relation[66]

$$|\Psi^{(n)}\rangle = \begin{cases} \hat{O}\,|\Psi\rangle & n=1 \\ 2\hat{O}\left|\Psi^{(n-1)}\right\rangle - \left|\Psi^{(n-2)}\right\rangle & n \geq 2 \end{cases} \tag{35}$$

where $\hat{O}$ is the modified (normalized) Hamiltonian

$$\hat{O} = 2\frac{\hat{H}_{\mathrm{Q}} - \epsilon_{\mathrm{min}}\hat{\mathbb{1}}_{\mathrm{s}}}{\delta_E} - \hat{\mathbb{1}}_{\mathrm{s}}. \tag{36}$$

The action of $\hat{O}$ on $|\Psi\rangle$ is the same as $\hat{H}_{\mathrm{Q}}$ on $|\Psi\rangle$ as described in Eq. 28, with the coefficients now scaled according to Eq. 36.

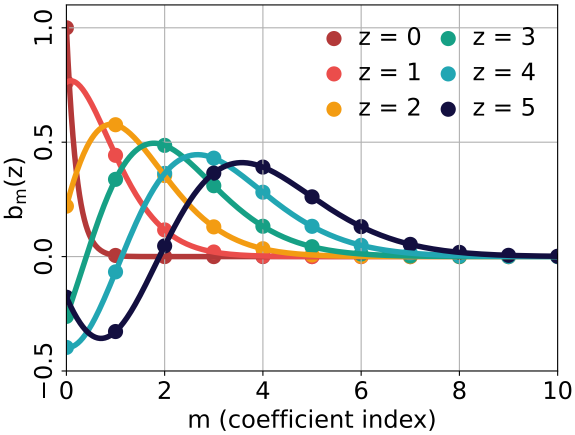

FIG. 2. The Chebyshev coefficients as a function of expansion index for various uncertainty parameters, z. The colored curves represent the bessel function for a continuous "m" coordinate and the dots are the bessel functions evaluated at integer "m" values.

Fig. 2 presents the magnitude of the Chebyshev coefficients as a function of the expansion term index for various z-values. With an increase in z, more terms are needed for the expansion to converge. For $z \ll 1$, only the first three or four terms in the expansion are required. For comparison, a typical propagation scheme such as RK-4 or a symplectic integrator (velocity verlet) typically needs a much smaller substep, $\delta t \approx \Delta t/10 - \Delta t/100$ for a stable integration of the dynamics. The Chebyshev expansion approach thus provides a significant speedup of the dynamics propagation compared to solving Eq. 31 using RK4 because one can use a much larger Δt (up to 100 times), with only a slight increase of the prefactor of the computational cost associated with how many terms are needed to form a converged Chebyshev expansion (each associated with the $\hat{O}|\Psi\rangle$ operations). In all simulations, we are in the regime of $z \ll 1$ and we found that only $n = 4$ terms of the Chebyshev polynomial are required to converge the results.

C. Decomposing Single and Double excitation Subspace

The inclusion of a double excitation subspace can make our δ_E very large, forcing us to choose a very small Δt. Note that the double-excitation subspace has a diagonal energy that is about twice that of the single-excitation subspace (when it has zero light-matter detuning). Further, the Hamiltonian has a block-diagonal structure of $\hat{H}_{\mathrm{Q}}$, illustrated in Fig. 1, where the single and double excitation manifolds are not coupled to each other through Hamiltonian operators (they are connected through the dipole operator and will have transitions upon laser excitation). This observation leads us to separate the first and second excitation subspaces with their individual spectral radius. The operation $\hat{O}\,|\Psi\rangle$, via Eq. 28 is thus performed separately for the different subspaces. We separate the system Hilbert space into different excitation manifolds,

$$\hat{H}_{\mathrm{Q}} = \bigoplus_{\xi} \hat{H}^{(\xi)}, \tag{37a}$$

$$|\Psi\rangle = \bigoplus_{\xi} |\Psi^{(\xi)}\rangle, \tag{37b}$$

where $\xi = 0$ indicates the ground state (Eq. 22), and $\xi = 1$ and $\xi = 2$ indicate the single (Eq. 23) and double excitation manifold (Eq. 24), respectively. The quantum propagation can now be separated into the propagation of different subspaces

$$\hat{U}(\Delta t)\,|\Psi\rangle = \bigoplus_{\xi} \exp\left(\frac{-i\hat{H}^{(\xi)}\Delta t}{\hbar}\right)|\Psi^{(\xi)}\rangle. \tag{38}$$

We can now independently apply the Chebyshev expansion in different subspaces. For the first excitation subspace, the approximate spectral radius and lower-bound of the eigenvalue are given by

$$\delta_E^{(1)} = 2g_{\mathrm{c}}\sqrt{N} + 2\lambda_{\mathrm{b}} \tag{39a}$$

$$\epsilon_{\mathrm{min}}^{(1)} = \bar{\varepsilon} - g_{\mathrm{c}}\sqrt{N} - \lambda_{\mathrm{b}}, \tag{39b}$$

where $\bar{\varepsilon} = \sum_n \varepsilon_n/N$, and λ_{b} is the bath reorganization energy that accounts for the bath fluctuations. For the second excitation manifold, these quantities are[10,48,49]

$$\delta_E^{(2)} = 2g_{\mathrm{c}}\sqrt{2(N-1)} + 4\lambda_{\mathrm{b}} \tag{40a}$$

$$\epsilon_{\mathrm{min}}^{(2)} = 2\bar{\varepsilon} - g_{\mathrm{c}}\sqrt{2(N-1)} - 2\lambda_{\mathrm{b}}, \tag{40b}$$

where we used the analytic results[10,48,49] to estimate the lower bound of the polariton eigenstate as $2\bar{\varepsilon} - g_{\mathrm{c}}\sqrt{2(N-1)}$ in Eq. 40b.

The Chebyshev expansion allows efficient dynamics propagation by accurately calculating the action of the unitary propagator on an arbitrary vector. However, there is still a numerical challenge in simulating quantum dynamics with the HTC model. In Eq. 34, the phase factor in the Chebyshev expansion, Eq. 32, depends on the approximate absolute magnitude of the lower eigenvalue ϵ_{min}. Thus, if the eigenvalue has a large absolute magnitude, the accuracy of this method is reduced due to the noise that builds up from the highly oscillating term coming from the high absolute magnitude of ϵ_{min}, especially if we are simulating both ground state and single excitations (or further including the double excitation) where these values are on the order of eV, and the difference between $\epsilon^{(1)}_{\text{min}}$ and $\epsilon^{(2)}_{\text{min}}$ are also on the order of eV. The same challenge also exists in other propagation methods, such as using RK4 to solve Eq. 17, because when a large energy difference exists in a Hamiltonian, one would need a much smaller Δt to fully capture the phase oscillations when propagating the coefficients.

This numerical challenge can be easily resolved by decomposing the Hamiltonian as $\hat{H} = \bar{\varepsilon}\hat{\mathbb{1}} + \Delta\hat{H}$, where $\bar{\varepsilon}$ is a *constant* reference energy level, and $\Delta\hat{H}$ is the fluctuation around $\bar{\varepsilon}$. Because $\bar{\varepsilon}\hat{\mathbb{1}}$ commute with $\Delta\hat{H}$, the quantum evolution becomes $e^{-\frac{i}{\hbar}\hat{H}\Delta t} = e^{-\frac{i}{\hbar}\bar{\varepsilon}\Delta t}\cdot e^{-\frac{i}{\hbar}\Delta\hat{H}\cdot\Delta t}$, where the highly oscillatory part of the phase $e^{-\frac{i}{\hbar}\bar{\varepsilon}\Delta t}$ will be evaluated analytically, and the rest of the propagation $e^{-\frac{i}{\hbar}\Delta\hat{H}\cdot\Delta t}$ will be numerically updated using the Chebyshev expansion. Further, in the HTC Hamiltonian, these subspaces are not directly connected by Hamiltonian terms. Following this logic, we rewrite the Hamiltonian in Eq. 37a as

$$\hat{H}_{\text{Q}} = \hat{H}^{(0)} \oplus (\bar{\varepsilon}\hat{\mathbb{1}}^{(1)}_{\text{s}} + \Delta\hat{H}^{(1)}) \oplus (2\bar{\varepsilon}\hat{\mathbb{1}}^{(2)}_{\text{s}} + \Delta\hat{H}^{(2)}) \tag{41}$$

where $\hat{\mathbb{1}}^{(\xi)}_{\text{s}}$ is the identity operator of the ξ_{th} excitation subspace and $\Delta\hat{H}^{(\xi)} = \hat{H}^{(\xi)} - (\xi\bar{\varepsilon})\cdot\hat{\mathbb{1}}^{(\xi)}_{\text{s}}$, and where $\xi\bar{\varepsilon}$ is the reference energy for the ξ_{th} excitation subspace (*i.e.*, $\bar{\varepsilon}$ for single excitation and $2\bar{\varepsilon}$ for double excitation subspace). Since the identity operator commutes with any other operators in its respective subspace, using Eq. 41, the propagator now becomes

$$\hat{U}(\Delta t)\,|\Psi\rangle = \bigoplus \exp\Big(\frac{-i\xi\bar{\varepsilon}\Delta t}{\hbar}\Big)\exp\Big(\frac{-i\Delta\hat{H}^{(\xi)}\cdot\Delta t}{\hbar}\Big)|\Psi^{(\xi)}\rangle, \tag{42}$$

where the $\exp\Big(-\frac{i}{\hbar}\Delta\hat{H}^{(\xi)}\Delta t\Big)|\Psi^{(\xi)}\rangle$ update will be performed using the Chebyshev expansion, and then multiply with a phase $\exp(-\frac{i}{\hbar}\xi\bar{\varepsilon}\Delta t)$. With this separation, the accuracy of the Chebyshev propagator is independent of the absolute value of electronic excitation energies. For the Chebyshev expansion with the shifted eigenvalues, the approximate lower eigenvalues used in Eq. 36 is now

$$\epsilon^{(1)}_{\text{min}} = -g_{\text{c}}\sqrt{N} - \lambda_{\text{b}} \tag{43}$$

$$\epsilon^{(2)}_{\text{min}} = -g_{\text{c}}\sqrt{2(N-1)} - 2\lambda_{\text{b}} \tag{44}$$

whereas the $\delta^{(\xi)}_{E}$ (as expressed in Eq. 39a and Eq. 40a) remains unchanged. Because different subspaces are not directly coupled by $\hat{H}_{\text{Q}}$, when propagating the quantum dynamics governed by H_{Q}, the above Chebyshev scheme will be used independently for each subspace. On the other hand, different subspaces are connected through the cavity loss process (such as $|\text{G}^1\rangle \to |\text{G}^0\rangle$ in the single excitation subspace, and $|\text{G}^2\rangle \to |\text{G}^1\rangle$ and $|\text{E}^1_n\rangle \to |\text{E}^0_{nm}\rangle$ in the double excitation space), and when computing the response function, the instantaneous action of the dipole operator will connect them. For those two types of operations, one will apply the stochastic Lindblad algorithm (Appendix A) and the rule of dipole on state vector directly, without shifting the reference energies. This simple technique outlined in Eq. 42 significantly reduces the noise of the numerical propagation and increases the accuracy of the Chebyshev expansion method, as shown in Appendix B.

D. Spectroscopy Simulations and Efficient Evaluation of the $\hat{\mu}|\Psi\rangle$ Operation

Within the linear response limit, the absorption spectra of a system can be expressed as the dipole-dipole auto-correlation function[25,41,44,47]

$$R^{(1)}(t_1) = i\text{Tr}[\hat{\mu}(t_1)[\hat{\mu}(0), \hat{\rho}_0]], \tag{45}$$

where the laser excitation is applied at time $t = 0$, and one detects the system response at time t_1. The trace is performed for all DOFs. In addition, $\hat{\rho}_0$ represents the initial density matrix of the entire system in equilibrium ground state at $t = -\infty$, ($\hat{\rho}_0 = \hat{\rho}(-\infty)$). Further, $\hat{\rho}_0$ is assumed to be a separable state between the polariton and the phonon bath DOFs as follows

$$\hat{\rho}_0 = \hat{\rho}_g \otimes \hat{\rho}_{\text{b}} = |\text{G}^0\rangle\langle\text{G}^0| \otimes \hat{\rho}_{\text{b}} = |\text{G}^0\rangle\langle\text{G}^0| \otimes \frac{e^{-\beta\hat{H}_{\text{b}}}}{\mathcal{Z}}, \tag{46}$$

with $|\text{G}^0\rangle$ defined in Eq. 22.

The frequency domain spectra can be computed by

$$R^{(1)}(\omega) = \int_0^T dt e^{i\omega t} R^{(1)}(t)\cos\left(\frac{\pi t}{2T}\right), \tag{47}$$

where T is the maximum time of the recorded time-domain spectra and $\cos(\pi t/2T)$ is a smoothing function.[25,47]

As can be seen, to compute $R^{(1)}(t_1)$ and $R^{(1)}(\omega)$, one needs to act the dipole operator, $\hat{\mu}$, on the density matrix, which in principle also scales as $\mathcal{O}(\mathcal{K}^4)$. However, $\hat{\mu}$ also takes the form of a very sparse matrix in the single and double excitation subspace, as illustrated in Fig. 3. The sparsity of the dipole operator scales as $1 - 1/N^2$ with N molecules coupled to a cavity mode. The action of $\hat{\mu}$ on a ket vector (following the same arrangement of the basis as in Eq. 25) can be written as

$$\hat{\mu}|\Psi\rangle = \sum_n \mu_n c_{\text{E}^0_n}|\text{G}^0\rangle + \sum_n \Big(\mu_n c_{\text{G}^0} + \sum_{m>n}\mu_m c_{\text{E}^0_{nm}}\Big)|\text{E}^0_n\rangle + \left(\sum_n \mu_n c_{\text{E}^1_n}\right)|\text{G}^1\rangle + c_{\text{G}^1}\sum_n \mu_n|\text{E}^1_n\rangle \tag{48}$$

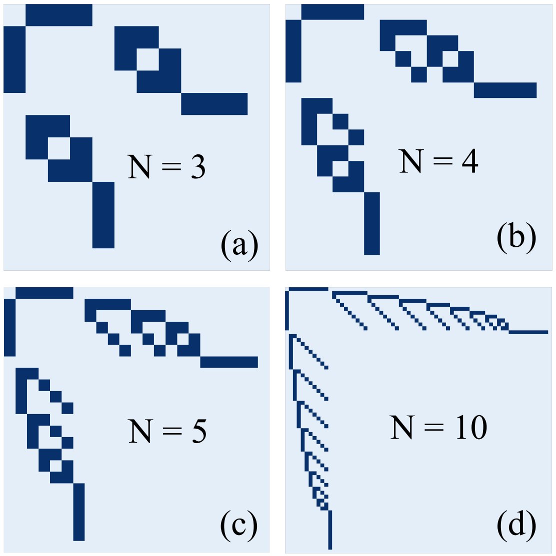

FIG. 3. Matrix representation of the Dipole operator $\hat{\mu}$ (see Eq. 48) for N molecules. The light cyan color represents the zero matrix elements, whereas the dark blue represents the non-zero matrix elements. Panels (a)-(d) show the Hamiltonian for 3, 4, 5, and 10 molecules, respectively, under the double excitation basis

.

The above becomes a very simplified modification of $|\Psi\rangle$,

$$\hat{\mu}|\Psi\rangle = \begin{bmatrix} \sum_n \mu_n c_{\mathrm{E}_n^0} \\ \mu_n c_{\mathrm{G}^0} + \sum_{m>n} \mu_m c_{\mathrm{E}_{nm}^0} \\ \sum_n \mu_n c_{\mathrm{E}_n^1} \\ \sum_{m>n} \mu_n c_{\mathrm{E}_{nm}^0} \\ \mu_n c_{\mathrm{G}^1} \\ 0 \end{bmatrix} \tag{49}$$

This helps to significantly reduce the cost of acting dipole operator on state vector in spectroscopy calculations.

IV. COMPUTATIONAL METHOD

A. PLDM Approach for Dynamics Propagation

We briefly outline the PLDM approach for quantum dynamics simulations.[26,27,53,67] The diabatic Hamiltonian of a system coupled to a bath (nuclear DOF) can be expressed as

$$\begin{aligned}\hat{H} &= \frac{\hat{P}^2}{2M} + V_0(\hat{R}) + \sum_a^{\mathcal{K}} V_{aa}(\hat{R})\,|a\rangle\langle a| + \frac{1}{2}\sum_{b\neq a}^{\mathcal{K}} V_{ab}(\hat{R})\,|a\rangle\langle b| \\ &= \hat{H}_{\mathrm{b}} + \hat{H}_{\mathrm{Q}}. \end{aligned} \tag{50}$$

where $\hat{R}$ and $\hat{P}$ are the position and momenta, respectively, of the bath particles of mass M, and $V_0(\hat{R})$ is the state-independent part of the Hamiltonian. In the context of this work

$$\begin{aligned}\hat{H}_{\mathrm{b}} &= \frac{\hat{P}^2}{2M} + V_0(\hat{R}), \\ \hat{H}_{\mathrm{Q}} &= \sum_a^{\mathcal{N}} V_{aa}(\hat{R})\,|a\rangle\langle a| + \frac{1}{2}\sum_{b\neq a}^{\mathcal{N}} V_{ab}(\hat{R})\,|a\rangle\langle b|\,, \end{aligned}$$

where $\hat{H}_{\mathrm{Q}}$ is the quantum part of the Hamiltonian that include $\hat{H}_{\mathrm{s}}$ and $\hat{H}_{\mathrm{sb}}$ (Eq. 16).

Using Meyer-Miller-Stock-Thoss (MMST) mapping procedure,[56,68,69] we get the *classical* mapping Hamiltonian[26]

$$\begin{aligned}\mathcal{H}(R,\mathbf{x},\mathbf{p}) =& \frac{P^2}{2M} + V_0(R) + \frac{1}{2}\sum_a V_{aa}(R)(x_a^2 + p_a^2) \\ &+ \frac{1}{2}\sum_{b\neq a} V_{ab}(R)(x_a x_b + p_a p_b). \end{aligned} \tag{51}$$

For a given set of the system operator $\hat{A}$ and $\hat{B}$, and $\hat{\rho}_{\mathrm{b}}$ is the initial bath density operator, the time evolution of the PLDM is

$$\begin{aligned}C_{AB}(t) &= \mathrm{Tr}\left[\hat{\rho}_{\mathrm{b}} \otimes \hat{A} e^{\frac{i}{\hbar}\hat{H}t} \hat{B} e^{-\frac{i}{\hbar}\hat{H}t}\right] \\ &\approx \sum_{jk,ab} \int d\tau [\hat{\rho}_{\mathrm{b}}]_{\mathrm{w}} \cdot [\hat{A}]_{jk} \cdot \mathcal{T}_{ka}(t) \cdot [\hat{B}]_{ab} \cdot \tilde{\mathcal{T}}_{bj}(t), \end{aligned} \tag{52}$$

where

$$d\tau \equiv dR \cdot dP \cdot d\mathbf{x} \cdot d\mathbf{p} \cdot d\tilde{\mathbf{x}} \cdot d\tilde{\mathbf{p}} \cdot G \cdot \tilde{G}, \tag{53}$$

$\mathbf{x} \equiv \{x_a\}$ and $\mathbf{p} \equiv \{p_a\}$ are the mapping variables associated with the forward propagator, and $\tilde{\mathbf{x}}$ and $\tilde{\mathbf{p}}$ are for the backward propagator, both of which evolving according to the classical mapping Hamiltonian $\mathcal{H}(R,\mathbf{x},\mathbf{p})$ in Eq. 51. Further, $G = \exp\left[-\frac{1}{2}\sum_a ({p_a}^2 + {x_a}^2)\right]$ is the Gaussian distribution for the initial forward mapping variables, with an analogous expression $\tilde{G}$ for backward mapping variables. In addition,

$$\mathcal{T}_{b,j}(t) = \frac{1}{2}(x_b(t) + ip_b(t))(x_j(0) - ip_j(0)) \tag{54a}$$

$$\tilde{\mathcal{T}}_{k,a}(t) = \frac{1}{2}(\tilde{x}_k(t) - i\tilde{p}_k(t))(\tilde{x}_a(0) + i\tilde{p}_a(0)) \tag{54b}$$

are the transition amplitudes associated with the forward and backward propagator, respectively. The initial bath distribution is obtained by sampling from the Wigner density

$$[\hat{\rho}_{\mathrm{b}}]_{\mathrm{w}} = \int d\Delta e^{-\frac{i}{\hbar}RP} \left\langle R - \frac{\Delta}{2}\,|\hat{\rho}_{\mathrm{b}}|\, R + \frac{\Delta}{2} \right\rangle. \tag{55}$$

Here, R and P denote the mean position of the bath and the momentum. The system mapping variables (for both forward and backward variables) evolve according to Hamilton's EOM

$$\frac{\partial x_a}{\partial t} = \frac{\partial \mathcal{H}}{\partial p_a} = \frac{1}{\hbar}\sum_b V_{ab}(R)p_b, \tag{56a}$$

$$\frac{\partial p_a}{\partial t} = -\frac{\partial \mathcal{H}}{\partial x_a} = -\frac{1}{\hbar}\sum_b V_{ab}(R)x_b, \tag{56b}$$

The bath DOF evolves classically

$$\frac{\partial R}{\partial t} = P, \quad \frac{\partial P}{\partial t} = \mathcal{F}, \tag{57a}$$

$$\mathcal{F}(R) = -\frac{1}{2}\nabla_R\left\{\mathcal{H}(R,\mathbf{x},\mathbf{p}) + \mathcal{H}(R,\tilde{\mathbf{x}},\tilde{\mathbf{p}})\right\}, \tag{57b}$$

and experiences a mean force from both forward and backward mapping variables.

Note that the EOM for the mapping variables is completely equivalent to the TDSE.[65] By establishing a transformation relation

$$x_a(t) = \sqrt{2}\cdot\mathfrak{Re}[c_a(t)]; \quad p_a(t) = \sqrt{2}\cdot\mathfrak{Im}[c_a(t)], \tag{58}$$

Eq. 56 is equivalent to the following TDSE

$$i\hbar\dot{c}_a(t) = \sum_b V_{ab}(R(t))\cdot c_b(t). \tag{59}$$

This was discussed by Gray and Manopolous as the Symplectic integrator of TDSE.[65] For the mapping approaches with an explicit zero point energy factor (such as SQC[60,61] and spin-LSC[57,58]), a similar argument can also be carried out (for example, Eqs. 94-95 in Ref. 57,58). Historically, the PLDM and related mapping dynamics approaches are often solved with a simple velocity verlet algorithm[70] or complete symplectic algorithm[71,72] (that requires diagonalizing $\hat{V}$), which are expensive to perform when having a large N in HTC Hamiltonian.

In this work, we use the relation between mapping variables and coefficients

$$c_a = \frac{1}{\sqrt{2}}(x_a + ip_a); \quad \tilde{c}_a = \frac{1}{\sqrt{2}}(\tilde{x}_a - i\tilde{p}_a) \tag{60}$$

and the mapping EOMs in Eq. 56 becomes

$$i\hbar\dot{c}_a(t) = \sum_b V_{ab}(R(t))\cdot c_b(t), \tag{61a}$$

$$-i\hbar\dot{\tilde{c}}_a(t) = \sum_b V_{ab}(R(t))\cdot \tilde{c}_b(t). \tag{61b}$$

Here, we take advantage of the Chebyshev series in Eq. 32, and the action of $\hat{H}_{\mathrm{Q}}$ on the state vector outlined in Eq. 28, as well as the subspace decomposition and energy shift techniques outlined in Eq. 41. The nuclear force of the PLDM approach (in Eq. 57b) for the HTC Hamiltonian is expressed as

$$\mathcal{F}(t) = -\sum_a \frac{1}{2}(|c_a(t)|^2 + |\tilde{c}_a(t)|^2)\cdot\nabla_R\langle a|\hat{H}_{\mathrm{sb}}|a\rangle - \nabla_R\hat{H}_{\mathrm{b}} \tag{62}$$

which is computed directly using the updated coefficients $\{c_a(t), \tilde{c}_a(t)\}$ and scales linearly with $\mathcal{K}$. Further, the transition amplitudes are also directly expressed as

$$\mathcal{T}_{b,j}(t) = c_b(t)\cdot c_j^*(0) \tag{63a}$$

$$\tilde{\mathcal{T}}_{k,a}(t) = \tilde{c}_k(t)\cdot\tilde{c}_a^*(0) \tag{63b}$$

which are directly computed with the forward and backward coefficients and then used to compute $C_{AB}(t)$ based on Eq. 51. For an arbitrary correlation function, the $C_{AB}(t)$ still have a full sum over the indices $\{j,k,a,b\}$, which can, in principle, be further reduced if $\hat{A}$ and $\hat{B}$ exhibit the same type of sparsity. This is indeed the case for the linear response function (dipole-dipole autocorrelation function) with $\hat{A} = \hat{\mu}\hat{\rho}_0$ and $\hat{B} = \hat{\mu}$, as we showed in Eq. 49.

B. PLDM simulation of the Linear Spectra

For the linear response function expressed in Eq. 52, one can rewrite it as the sum of two correlation functions

$$R^{(1)}(t_1) = i\mathrm{Tr}\left[\hat{\mu}(0)\hat{\rho}_0\hat{\mu}(t_1)\right] - i\mathrm{Tr}\left[\hat{\rho}_0\hat{\mu}(0)\hat{\mu}(t_1)\right], \tag{64}$$

where $\hat{\rho}_0 = \hat{\rho}_g\otimes\hat{\rho}_{\mathrm{b}}$ (see Eq. 46). This can then be calculated using the expression of the PLDM correlation function (Eq. 52) by choosing $\hat{A} = \hat{\mu}(0)\hat{\rho}_g$, $\hat{B} = \hat{\mu}(t_1) = e^{\frac{i}{\hbar}\hat{H}t_1}\hat{\mu}e^{-\frac{i}{\hbar}\hat{H}t_1}$, and $\hat{A} = \hat{\rho}_g\hat{\mu}(0)$, $\hat{B} = \hat{\mu}(t_1) = e^{\frac{i}{\hbar}\hat{H}t_1}\hat{\mu}e^{-\frac{i}{\hbar}\hat{H}t_1}$. Alternatively, the response function can be expressed as[25,47]

$$\begin{aligned} R^{(1)}(t_1) &= i\mathrm{Tr}\left[\hat{\mu}(t_1)\hat{\mu}\hat{\rho}_g\right] - i\mathrm{Tr}\left[\hat{\mu}(t_1)\hat{\rho}_g\hat{\mu}\right] \\ &= i\mathrm{Tr}\left[\hat{\mu}e^{\frac{i}{\hbar}\hat{H}t_1}(\hat{\mu}\hat{\rho}_0)e^{-\frac{i}{\hbar}\hat{H}t_1}\right] - i\mathrm{Tr}\left[\hat{\mu}e^{\frac{i}{\hbar}\hat{H}t_1}(\hat{\rho}_0\hat{\mu})e^{-\frac{i}{\hbar}\hat{H}t_1}\right], \end{aligned} \tag{65}$$

which can be approximated by using the PLDM approach as follows[25]

$$\begin{aligned} R^{(1)}(t_1) \approx\; & i\sum_{n_1}\sum_{n_0,\tilde{n}_0}\int d\tau_0[\hat{\mu}\tilde{\rho}^{(1)}]_{n_1,n_1}[\hat{\mu}\hat{\rho}_g]_{n_0,\tilde{n}_0}\cdot[\hat{\rho}_{\mathrm{b}}]_{\mathrm{w}} \\ & - i\sum_{n_1}\sum_{n_0,\tilde{n}_0}\int d\tau_0[\hat{\mu}\tilde{\rho}^{(1)}]_{n_1,n_1}[\hat{\rho}_g\hat{\mu}]_{n_0,\tilde{n}_0}\cdot[\hat{\rho}_{\mathrm{b}}]_{\mathrm{w}}, \end{aligned} \tag{66}$$

where $\tilde{\rho}^{(1)}$ accounts for the transition amplitude from both forward and backward mapping trajectories, with the matrix elements expressed as follows

$$\begin{aligned} &[\tilde{\rho}^{(1)}]_{n_1\tilde{n}_1}(t_1, n_0, \tilde{n}_0) \\ =&\frac{1}{2}\left[x_{n_1}(t_1) + ip_{n_1}(t_1)\right]\cdot\left[x_{n_0}(0) - ip_{n_0}(0)\right] \\ &\times\frac{1}{2}\left[\tilde{x}_{\tilde{n}_1}(t_1) - i\tilde{p}_{\tilde{n}_1}(t_1)\right]\cdot\left[\tilde{x}_{\tilde{n}_0}(0) + i\tilde{p}_{\tilde{n}_0}(0)\right]. \end{aligned} \tag{67}$$

The linear response at time t_1 is obtained by performing a trace over $\hat{\mu}\tilde{\rho}^{(1)}$. Using Eq. 49 and Eq. 67, this becomes,

$$\begin{aligned}
&\sum_{n_1}^{N}[\hat{\mu}\tilde{\rho}^{(1)}]_{n_1 n_1}(t_1, n_0, \tilde{n}_0) \qquad (68)\\
&=\sum_{n_1}^{N}\mu_{n_1}\cdot\frac{1}{2}\left[x_{n_1}(t_1)+ip_{n_1}(t_1)\right]\cdot\left[x_{n_0}(0)-ip_{n_0}(0)\right]\\
&\quad\times\frac{1}{2}\left[\tilde{x}_{n_1}(t_1)-i\tilde{p}_{n_1}(t_1)\right]\cdot\left[\tilde{x}_{\tilde{n}_0}(0)+i\tilde{p}_{\tilde{n}_0}(0)\right]\\
&=\sum_{n_1}^{N}\left(\mu_{n_1}\cdot c_{n_1}(t_1)\cdot c^{*}_{n_0}(0)\right)\cdot\left(\tilde{c}_{n_1}(t_1)\cdot\tilde{c}^{*}_{\tilde{n}_0}(0)\right),
\end{aligned}$$

where in the last line we used the expression from Eq. 60.

The cavity loss dynamics is simulated using the stochastic Lindblad approach with PLDM, as detailed in Ref. 47. For a cavity mode with loss rate Γ, the Lindblad loss dynamics is equivalent to updating the forward and backward coefficients outlined in Eq. A3 and Eqs. A5-A6. For any $t \in [0, t_1 - \Delta t]$, the overall propagation of the reduced density matrix for the quantum subsystem during a time step Δt can thus be summarized as

$$\hat{\rho}(t+\Delta t) = \left[e^{\mathcal{L}_{\hat{L}}\Delta t/2}\cdot e^{\mathcal{L}_{\hat{H}}\Delta t}\cdot e^{\mathcal{L}_{\hat{L}}\Delta t/2}\right]\hat{\rho}(t), \qquad (69)$$

where $e^{\mathcal{L}_{\hat{L}}}$ is the decay dynamics propagation according to the stochastic Lindblad approach, and $e^{\mathcal{L}_{\hat{H}}}$ is the PLDM propagation in Eq. 61, coupled to the nuclear update with the force described in Eq. 62. In the current work, the PLDM update $e^{\mathcal{L}_{\hat{H}}\Delta t}$ is performed using the Chebyshev Series Expansion outlined in Sec. III B, and the nuclear update is performed using velocity verlet. The stochastic Lindblad update $e^{\mathcal{L}_{\hat{L}}}$ is performed using as outlined in Eq. A3 and Eqs. A5-A6 for $\Delta t/2$ before and after the PLDM propagation. We refer to Eq. 69 as the $\mathcal{L}-$PLDM approach.[47] Note that although we formally express the propagation as the reduced density matrix in Liouville space, all of the dynamical propagation has been performed in Hilbert space for the forward and backward coefficients.

To evaluate the matrix element $[\hat{\mu}\hat{\rho}_g]_{n_0,\tilde{n}_0}$, the action of the dipole operator on the ground state can be expressed as

$$\hat{\mu}\hat{\rho}_g = \sum_{n}\mu_n|\mathrm{G}^0\rangle\langle\mathrm{E}^0_n|, \qquad (70)$$

which is only non-zero for N off-diagonal elements. However, the final expression of $R^{(1)}$ requires a sum of $\sum_{n_0,\tilde{n}_0}$. To further reduce the cost, we use the focusing algorithm and the stochastic important sampling[25] to obtain the initial mapping variables, which, upon trajectory average, results in the same answer as if explicitly performing the sum $\sum_{n_0,\tilde{n}_0}$. For each trajectory, we use the focused initial condition for the mapping variables, with $c_{\mathrm{G}_0} = 1$, $c_{\mathrm{E}^0_i} = 0$ ($\forall\ i \in [1, N]$), $\tilde{c}_{\mathrm{G}_0} = 0$, $\tilde{c}_{\mathrm{E}^0_i} = 0$ ($\forall\ i \in [1, N]$ and $i \neq n$,) and $\tilde{c}_{\mathrm{E}^0_n} = 1$, and the focusing label n is stochastically chosen with the probability $P(n) = \mu_n/(\sum_{m=1}^{N}\mu_m)$ and initialize $c_{\mathrm{G}^0} = \tilde{c}_{\mathrm{E}^0_n} = 1$.

The first term in Eq. 66 can be computed using the following steps

1. Sample the nuclear configuration based on $[\hat{\rho}_{\mathrm{b}}]_{\mathrm{w}}$. The state $|\mathrm{G}^0\rangle\langle\mathrm{E}^0_n|$ is randomly chosen for the focused initial condition, based on the algorithm outlined in the previous paragraph. Set the initial electronic condition $c_{\mathrm{G}_0} = 1$ and $\tilde{c}_{\mathrm{E}^0_n} = 1$, based on the focused initial condition, with $n_0 = \mathrm{G}^0$ and $\tilde{n}_0 = \mathrm{E}^0_n$, and the rest of the coefficients to be zero.

2. Propagate the dynamics based on Eq. 69. In particular, for the $e^{\mathcal{L}_{\hat{H}}\Delta t}$ part, use Eq. 61 to propagate the forward and backward electronic coefficients, and Eq. 62 to compute the nuclear force to update nuclear DOFs; for the $e^{\mathcal{L}_{\hat{L}}\Delta t_k/2}$ part, use Eq. A3 to update the coefficients to describe the Lindblad loss dynamics.

3. Compute the first term of the response function based on the estimator $i\sum_{n_1}[\hat{\mu}\tilde{\rho}^{(1)}]_{n_1,n_1}\cdot[\hat{\mu}\hat{\rho}_g]_{n_0,\tilde{n}_0}$ where the initial label of the states are $n_0 = \mathrm{G}^0$ and $\tilde{n}_0 = \mathrm{E}^0_n$, and explicitly compute the trace $\sum_{n_1}$ by summing all terms expressed in Eq. 68. Average the correlation function from an ensemble of trajectories (for the $\int d\tau_0$ integral) to get the linear response signal.

For the second term, one can simply take the complex conjugate of the first term to reduce some computational costs. However, we directly compute both terms in this work (as well as in our previous work[47]) and add them together. This generates the $R^{(1)}(t_1)$, with examples provided in Fig. 4. Further perform the Fourier transform (see Eq. 47) of $R^{(1)}(t_1)$ generates the $R^{(1)}(\omega)$.

C. Model Systems and Computational Details

In all simulations, we use the HTC Hamiltonian for N molecules coupled to the cavity. Each molecule is coupled to an independent phonon bath, discretized by $N_\nu = 20$ independent bath modes from the Debye spectral density (see Eq. 9). The bath parameters are sampled using the procedure outlined in Ref. 27 (or more generally, Ref. 40)

$$C_\nu = 2\sqrt{\frac{\lambda}{\pi N_\nu \omega_\nu}\tan^{-1}\left(\frac{\omega_{\max}}{\omega_{\mathrm{b}}}\right)}, \qquad (71a)$$

$$\omega_\nu = \omega_{\mathrm{b}}\tan\left[\frac{\nu}{N_\nu}\tan^{-1}\left(\frac{\omega_{\max}}{\omega_{\mathrm{b}}}\right)\right], \qquad (71b)$$

where $\omega_{\max} \gg \omega_{\mathrm{b}}$ is the maximum frequency when discretizing the bath frequencies. To sample within the classical regime, we choose $\omega_{\max} = 5\ \omega_{\mathrm{b}}$. The bath parameters are $\omega_{\mathrm{b}} = 18\ \mathrm{cm}^{-1}$ (which is 2.2 meV) and

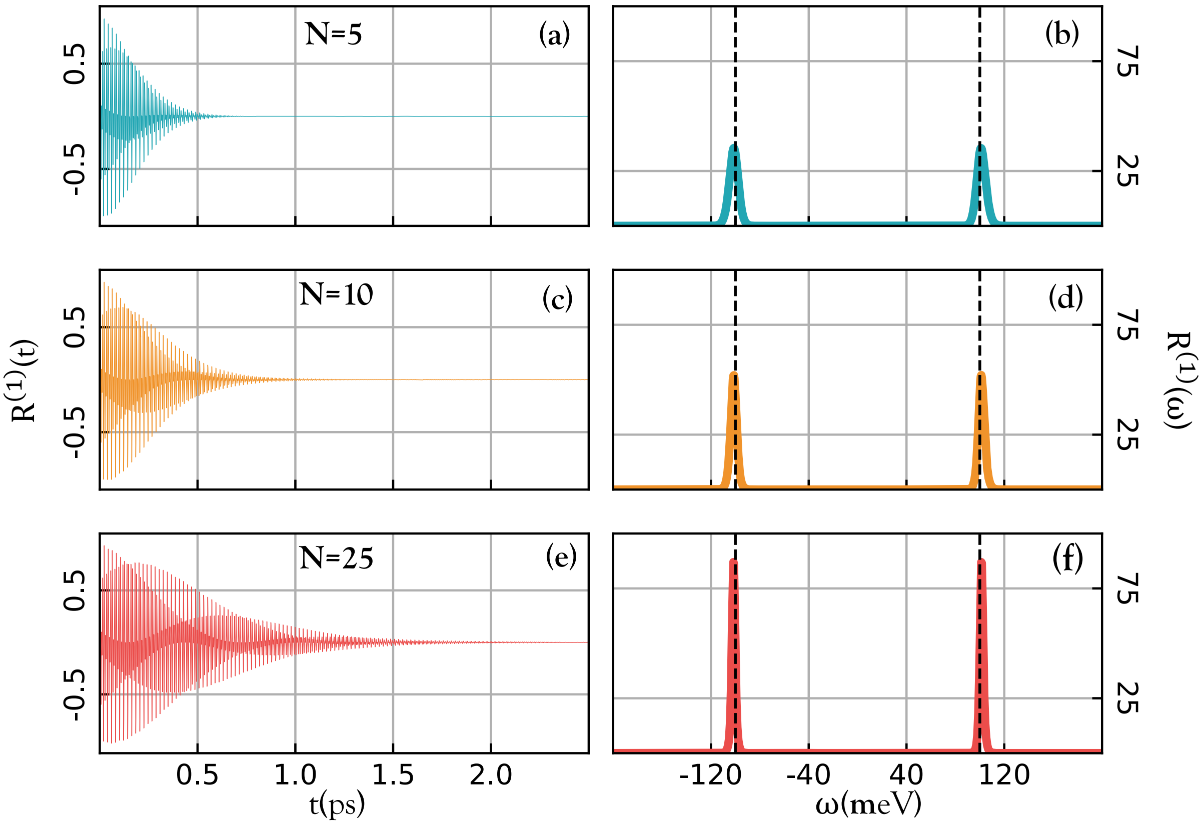

FIG. 4. Linear response function $R^{(1)}(t)$ as well as the spectra $R^{(1)}(\omega)$ of the HTC model, with different numbers of molecule N obtained from PLDM. Here, the collective Rabi splitting is fixed at $\hbar\Omega_{\mathrm{R}} = 0.2$ eV and there is no cavity loss. Panels (a), (c), and (e) represent the time-dependent polaritonic linear response for $N = 5, 10,$ and 25 molecules coupled to the cavity, respectively. Panels (b), (d), and (f) represent the normalized (by area) linear absorption spectra for $N = 5, 10,$ and 25 molecules coupled to the cavity respectively.

.

$\lambda_{\mathrm{b}} = 50$ cm^{-1} (which is 6.2 meV). The characteristic phonon frequency ω_{b} leads to a bath correlation function decay timescale of 300 fs. The initial bath condition $\hat{\rho}_{\mathrm{b}}$ (see Eq. 55) is described by its Wigner transform with the following analytic expression,

$$[\hat{\rho}_{\mathrm{b}}]_{\mathrm{w}} = \prod_{\nu} 2\tanh\left(\frac{\beta\hbar\omega_{\nu}}{2}\right) \times \exp\left[-\tanh\left(\frac{\beta\hbar\omega_{\nu}}{2}\right)\left(\frac{\omega_{\nu}^{2}R^{2}}{\hbar^{2}} + \frac{P^{2}}{\hbar^{2}\omega_{\nu}^{2}}\right)\right]. \tag{72}$$

The temperature is taken to be 300 K for all simulations with $\beta = 1052.58$ au.

To perform linear spectra calculations, we remain within the single excited subspace described in Eq. 22 and Eq. 23. For a demonstration of linear response signals at different N coupled to the cavity (Fig. 4), we fix the magnitude of the collective Rabi-splitting, $\hbar\Omega_{\mathrm{R}} = 2\sqrt{N}\hbar g_{\mathrm{c}} = 0.2$ eV. For the molecules, we used the average excitation energy of $\varepsilon_n = \bar{\varepsilon} = 0.5$ eV. The cavity frequency is also kept at $\hbar\omega_{\mathrm{c}} = 0.5$ eV (zero light-matter detuning). The cavity is lossless with $\Gamma = 0$ meV.

To simulate disorder effects in linear spectra (Figs. 6-7), we fix the collective coupling strength $2\sqrt{N}\hbar g_{\mathrm{c}}$ at 0.2 eV for $N = 500$ molecules. For the molecules, we used the average excitation energy of $\bar{\varepsilon} = 2.0$ eV. Throughout this work, we consider the resonance condition where

$$\bar{\varepsilon} = \hbar\omega_{\mathrm{c}}, \tag{73}$$

where we have ignored the solvent reorganization energy λ_{b} (see Eq. 9) in the above condition due to its small value. For Fig. 6, ε_n is sampled based on a Gaussian distribution (Eq. 74), while $\bar{\varepsilon} = 2.0$ eV. For results presented in Fig. 7), there is no site energy disorder and $\varepsilon_n = \bar{\varepsilon} = 2.0$ eV. The cavity frequency is thus kept at $\hbar\omega_{\mathrm{c}} = 2.0$ eV (zero light-matter detuning). The cavity loss rate was set at $\Gamma = 10$ meV. The nuclear time step for verlet propagation was taken to be $\Delta t = 10$ a.u. (≈ 0.25 fs), and the forward and backward coefficients are evolved between nuclear propagation using Eq. 32.

For energy disorder simulations (Fig. 6), the excitation energy for n_{th} molecule is sampled from the Gaussian

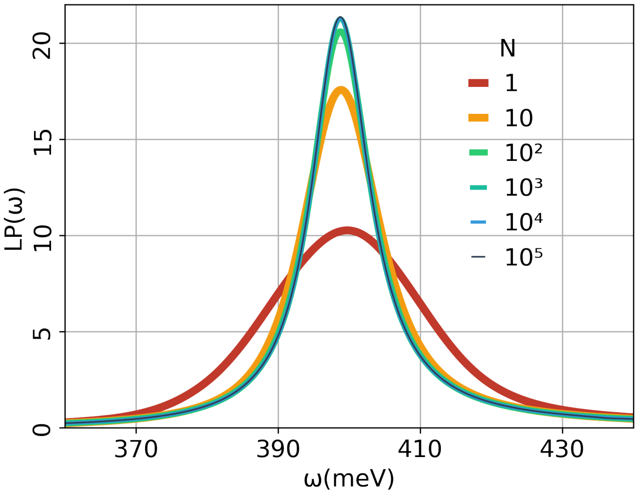

FIG. 5. Convergence of the lower polariton spectra with an increasing number of molecules from $N = 1$ to $N = 10^5$, while fixing $\hbar\Omega_\mathrm{R} = 2\sqrt{N}\hbar g_\mathrm{c} = 0.2$ eV a constant (by decreasing g_c accordingly). Here, we do not consider any type of disorder, and the cavity loss rate is set to be $\Gamma = 20$ meV.

distribution

$$P(\varepsilon_n) = \frac{1}{\sqrt{2\pi\sigma_\varepsilon^2}} e^{-(\varepsilon_n - \bar{\varepsilon})^2/2\sigma_\varepsilon^2} \tag{74}$$

where σ_ε is the width of the Gaussian centered at $\bar{\varepsilon}$. This introduces static inhomogeneity within the molecular excitation energies. The sampling is performed independently for each trajectory.

Following the previous work,[38] we also study the effect of orientation disorder by sampling the molecular orientation (with respect to the cavity mode) from Gaussian distribution,

$$P(\theta_n) = \frac{1}{\sqrt{2\pi\sigma_\theta^2}} e^{-(\theta_n - \bar{\theta})^2/2\sigma_\theta^2}. \tag{75}$$

The disorders in $\{\theta_n\}$ will influence the molecule-cavity coupling in Eq. 6. In the limit of $\sigma_\theta \to \infty$, it corresponds to an isotropic distribution of $\theta_0 \in [0, \pi]$ relative to the polarization direction of the cavity field. The expectation value of $\cos^2\theta$ for the Gaussian distribution is

$$\langle \cos^2\theta \rangle = \int_{-\infty}^{\infty} d\theta P(\theta) \cdot \cos^2\theta = \frac{1}{2} + \frac{1}{2} e^{-2\sigma_\theta^2}. \tag{76}$$

Following the previous work,[38] we further assume that the external laser field $\mathbf{E}(t)$ in the linear spectra simulation has the same direction as the cavity polarization direction $\hat{\mathbf{e}}$, such that

$$\hat{\boldsymbol{\mu}} \cdot \mathbf{E}(t) = \sum_n^N \mu_n \cos\theta_n \cdot E(t). \tag{77}$$

This means that the $\hat{\mu}$ expression in $R^{(1)}(t_1)$ when considering dipole orientational disorders will be expressed as

$$\hat{\mu} = \sum_n^N \mu_n \cos\theta_n. \tag{78}$$

In this work, we assume that the dipole will remain in a two-dimensional plane and deviate from the field polarization direction $\hat{\mathbf{e}}$.

To ensure tight convergence of $R^{(1)}(t)$, we used a total of 10^6 trajectories, although typically a total of $10^3 - 5 \times 10^3$ trajectories will provide visually converged results. The propagation time step for the Chebyshev propagation was chosen as $\Delta t = 20$ a.u. (≈ 0.5 fs). Once having a converged $R^{(1)}(t)$, we perform the numerical Fourier transform

$$R^{(1)}(\omega) = \sum_{j=0}^{T/\Delta t} \Delta t \cdot e^{i\omega j \Delta t} R^{(1)}(j\Delta t) \cos\left(\frac{\pi \cdot j\Delta t}{2T}\right),$$

where T is chosen such that the $R^{(1)}(t)$ is sufficiently decay to zero. For Fig. 4, for all N, the response signal was simulated up to $T = 2.5$ ps, where $R^{(1)}(t) \to 0$. In Fig. 5, all response signals were simulated till $T = 800$ fs. In Fig. 6, the response signal for each energy disorder (Eq. 74) decay to 0 with different T. For no disorder case, $\sigma_\varepsilon = 0.0$ eV, we chose $T = 1.5$ ps. For $\sigma_\varepsilon = 0.03$ eV, 0.04 eV, 0.05 eV, 0.1 eV and 0.2 eV, we chose $T = 1$ ps, $T = 500$ fs, $T = 300$ fs, $T = 80$ fs and $T = 50$ fs, respectively. To simulate dipole disorder (Eq. 75), we set $T = 1.5$ ps for all σ_θ cases in Fig. 7.

V. RESULTS AND DISCUSSIONS

1. Linear Response Signal

Fig. 4 presents the time-dependent linear response signal, $R^{(1)}(t)$ and the linear absorption spectra, $R^{(1)}(\omega)$, simulated using the PLDM approach. In this figure, we do not account for any type of disorder, and we keep $\sqrt{N}\hbar g_\mathrm{c}$ a constant as we change N. Fig. 4a and Fig. 4b present the linear response signal and the linear absorption spectra for $N = 5$ molecules coupled to the cavity, respectively. For the $R^{(1)}(\omega)$ data, we shift the axis with respect to $\hbar\omega_0 = \bar{\varepsilon}$, so the spectra are centered around zero instead of $\bar{\varepsilon}$. A clear observation of the linear response signal indicates the presence of two types of oscillations that arise due to the two polaritonic transitions, $|\mathrm{G}^0\rangle \to |-\rangle$ and $|\mathrm{G}^0\rangle \to |+\rangle$, as observed in the two peaks in linear spectra at $\hbar\omega - \bar{\varepsilon} \approx -100$ meV and $\hbar\omega - \bar{\varepsilon} \approx 100$ meV, respectively. Due to symmetry, there is no optical transition from $|\mathrm{G}^0\rangle$ to the dark state manifold $\{|\mathrm{D}_k\rangle\}$.

Panels (c) and (d) in Fig. 4 correspond to the case for $N = 10$ molecules. Since the linear response signal is a direct measurement of the coherent oscillations between the upper and lower polariton states, compared to panel (a), we can observe an increase in the coherence lifetime

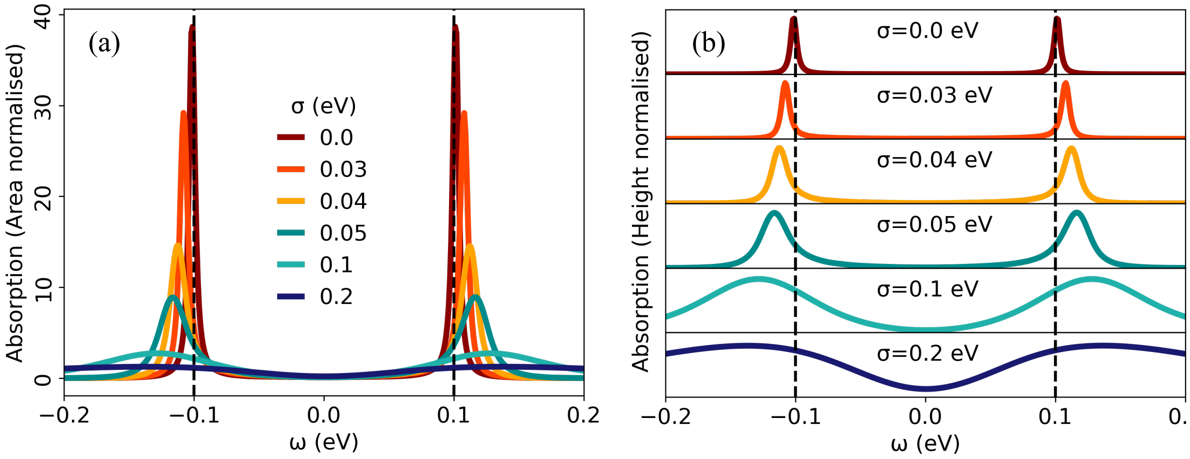

FIG. 6. Linear spectra of $N = 500$ molecules in the presence of various static energy disorders. (a) Polariton absorption spectra with each curve normalized with the corresponding area, and (b) represent the absorption curves with the peak height kept fixed. The plots are centered around the molecular excitation energy $\bar{\varepsilon} = 2.0$ eV. The black dotted lines are the analytical lower and upper polariton peaks for a system of N molecules coupled to a single cavity mode without any energy disorder.[39]

in $R^{(1)}(t)$ for the case of $N = 10$, which manifests itself as a further line width reduction and an increase in peak height for linear spectra $R^{(1)}(\omega)$, as shown in panel (d). This is due to the well-known polaron decoupling effect,[1,2,73] which effectively reduces the phonon reorganization energy by $\mathcal{O}(1/N)$ under the collective coupling regime (see Eq. 27 in Ref. 50 and the discussions there). Panels (e) and (f) present the results of coupling $N = 25$ molecules to the cavity mode, and we observe a further enhancement in the response signal lifetime and a further reduction in the polariton line widths.

In Fig. 5, we present the convergence of absorption lineshape with an increasing number of molecules from $N = 1$ to $N = 10^5$, while fixing the collective Rabi splitting, $\hbar\Omega_\mathrm{R} = 2\sqrt{N}\hbar g_\mathrm{c} = 0.2$ eV. We use a cavity loss rate of $\Gamma = 20$ meV and the same molecular parameters as used in Fig. 4. Fig. 5 presents the lower polariton lineshape for a different number of molecules. The LP spectra with $N = 10^2$ molecules (green curve) are visually close to the converged lineshape of $N = 10^5$ molecules (thin dark blue curve). From these curves, the lineshape features of linear spectroscopy due to collective effects appear to reach a convergence at $N \approx \mathcal{O}(10^2)$, which is very much closer to the lineshape features of $N = 10^5$. The theoretical approaches of this work allow us to directly perform the quantum dynamics and linear spectra simulations with $N = 10^5$ molecules and explore various trends of convergences.

2. Energy disorder

Fig. 6 presents the Linear absorption spectra of $N = 500$ molecules collectively coupled to the cavity, where each molecule is experiencing static energy disorder (inhomogeneous disorder), described in Eq. 74. Fig. 6a presents the absorption normalized with respect to the area, and Fig. 6b presents the absorption normalized with the intensity of the peak, with the vertical black dashed lines indicate the Rabi splitting without any static site energy disorders.

As the disorder in energy σ_ε approaches the same size of Rabi-splitting $\hbar\Omega_\mathrm{R} = 2\sqrt{N}\hbar g_\mathrm{c}$, one can observe that the effective Rabi-splitting slightly increases. This has been understood from perturbation theory,[38,74] where the effective Rabi splitting is expressed as $\hbar\Omega_\mathrm{R} \approx 2\sqrt{N}\hbar g_\mathrm{c} + \langle\delta\varepsilon\rangle^2/(\sqrt{N}\hbar g_\mathrm{c})$ when $\sigma_\varepsilon/(\sqrt{N}\hbar g_\mathrm{c}) \ll 1$ (see Appendix C of Ref. 38), as well as the approximate analytical solution of Rabi splitting when having Gaussian-type energy disorders.[74] As the line width increases with an increase in inhomogeneous disorder, the peak intensity decreases. This is because the effective number of molecules with zero detuning decreases. When further increasing the σ_ε to 0.2 eV (dark blue curve in Fig. 6a), the UP and LP peaks start to merge and the Rabi-splitting fades away. This pattern is clearer when we normalize the curves with the highest peak intensity, as shown in Fig. 6b. These observations also agree with the recent theoretical works.[38,74,75]

3. Dipole orientation disorder

Fig. 7 presents the linear spectra of $N = 500$ molecules coupled to a single cavity mode under various dipole orientation disorders based on Eq. 75, without any static energy disorders, $\varepsilon_n = \bar{\varepsilon} = \varepsilon$. We further center the spectra by setting $\hbar\omega_0 = \varepsilon = 0$. As one gradually increases the dipole orientation disorder σ_θ, Rabi splitting decreases. On the other hand, the linewidth of the polariton peaks remains almost unchanged, since there are no additional broadening mechanisms when including dipole disorders,

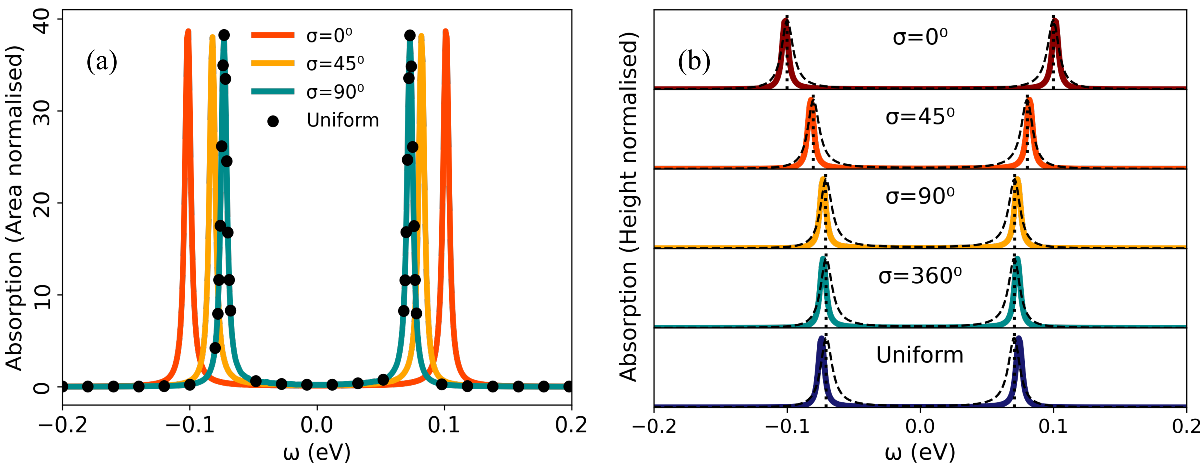

FIG. 7. Linear spectra of $N = 500$ molecules coupled to the cavity, in the presence of dipole orientation disorders. (a) Polariton absorption spectra with each curve normalized by area and (b) the same absorption spectra normalized by peak height. The plots are centered around the molecular excitation energy $\varepsilon_n = \bar{\varepsilon} = 2.0$ eV. The black dashed lines are the analytic result using Eq. 79. The vertical dotted lines indicate the effective Rabi splitting estimated from Eq. 80.

as opposed to the previous case when considering an inhomogeneous energetic disorder in the system.

For the resonance condition, $\hbar\omega_{\mathrm{c}} = \bar{\varepsilon}$, when considering the dipole orientation disorder, the polariton eigenspectrum is still analytically available.[37] By setting $\omega_0 = \omega_{\mathrm{c}}$, one can use the well-known analytic results of the lineshape[76] to expression absorption spectra as follows

$$R^{(1)}(\omega) = \frac{\Gamma\kappa N g_{\mathrm{c}}^2 \langle\cos^2\theta\rangle}{\left|(\omega - \omega_{\mathrm{c}} + i\frac{\Gamma}{2\hbar})(\omega - \omega_0 + i\frac{\kappa}{2\hbar}) - N g_{\mathrm{c}}^2\langle\cos^2\theta\rangle\right|^2}. \tag{79}$$

where κ is the molecular line width[47] and $\langle\cos^2\theta\rangle$ (see Eq. 76) is the effective modification of polariton frequencies depending on orientation disorder.[37,38]

In Fig. 7b, we present the numerical results obtained from our simulations (solid colors) when normalized to the peak height, as well as the analytic answer from Eq. 79 (black dashed lines). Overall, the analytic answer gives a reasonable estimate of the lineshape behavior across different angle disorders but slightly overestimates the linewidth. The narrower linewidth from the numerical results is likely due to the subaverage behavior[50,77,78] (linewidth smaller than $\Gamma/2 + \kappa/2$ for the resonant case, see Eq. 34 in Ref. 50), which cannot be captured by the simple expression of the lineshape in Eq. 79 that predicts the linewidth to be $\Gamma/2 + \kappa/2$ under the resonance case.

In Fig. 7b, we see that with an increase in dipole orientation disorder σ_θ, the effective Rabi-splitting decreases until it converges to a specific Ω_{R}. The convergence is reached around a disorder of $\sigma_\theta = 90°$. This can be interpreted as follows. For a HTC model Hamiltonian under the condition $\hbar\omega_{\mathrm{c}} = \bar{\varepsilon} = \varepsilon$, the polariton energies can be expressed as[37,39]

$$\varepsilon_\pm = \varepsilon \pm \frac{1}{2}\sqrt{4N\hbar^2 g_{\mathrm{c}}^2\langle\cos^2\theta\rangle + \left(-i\left[\frac{1}{2}\kappa - \frac{1}{2}\Gamma\right]\right)^2} \tag{80}$$

where $\langle\cos^2\theta\rangle$ is expressed in Eq. 76, λ_{b} is molecular reorganization energy (c.f. Eq. 9), which accounts for the additional light-matter detuning when the cavity frequency is equal to the bare molecular excitation. For the model system considered here, which is in the slow bath limit (inhomogeneous limit),[79] $\kappa/2 = \sqrt{\ln 2}\cdot\sqrt{\frac{\lambda_{\mathrm{b}} k_{\mathrm{B}}\mathrm{T}}{\hbar}}$, and $\sqrt{\ln 2}$ is the half of Full-width half maximum (FWHM) conversion factor for a Gaussian lineshape. The real part of Eq. 80 gives the location of the polariton peaks, and the imaginary part gives the linewidth of the respective polaritons.[39,47] For the resonance case, the Rabi splitting is expressed as

$$\hbar\Omega_{\mathrm{R}} = \mathrm{Re}[\varepsilon_+ - \varepsilon_-], \tag{81}$$

where $\varepsilon_\pm$ can be evaluated from Eq. 80. One can estimate the Rabi splitting and compare with the numerically simulated spectra. Indeed, the Rabi splitting decreases as one increases the dipole disorder from the fully aligned case (when $\sigma_\theta \to 0$ and thus $\langle\cos^2\theta\rangle = 1$) to the fully isotropic case in the 2D plane (when $\sigma_\theta \to \infty$ and thus $\langle\cos^2\theta\rangle = 1/2$). The vertical dashed line in each panel of Fig. 7b indicates the Rabi splitting based on the corresponding value of $\langle\cos^2\theta\rangle$ (cf. Eq. 76), and the numerical simulations agree well with the analytic result. The same behavior has also been discussed in (Appendix D) of Ref. 38.

VI. CONCLUSION

In this paper, we presented two general theoretical techniques for efficient simulation of polariton quantum dynamics under the collective light-matter coupling regime. The first one is related to the sparsity of the HTC Hamiltonian, which allows one to reduce the cost of acting polariton Hamiltonian onto a state vector to the linear order of the number of states, instead of the quadratic order. In principle, a direct density-matrix-based simulation requires a computational cost (in both time propagation and memory requirements) proportional to $\mathcal{O}(N^6)$, where N is the number of molecules and $\mathcal{O}(N^2)$ is the number of states in the double excitation subspace. The sparse nature of the HTC system Hamiltonian and dipole matrix allow for a compact expression of $\hat{H}_\mathrm{Q}|\Psi_\mathrm{s}\rangle$ and $\hat{\mu}|\Psi_\mathrm{s}\rangle$ as simple Hadamard products between vectors of $\mathcal{O}(N^2)$ instead of matrix-matrix or matrix-vector operations.

The theoretical technique applies the well-known Chebyshev series expansion approach for quantum dynamics propagation and uses it to simulate the polariton dynamics in the HTC system. The Chebyshev expansion allows us to use a much larger time step for propagation and only requires a few recursive operations of the Polariton Hamiltonian acting on state vectors, which we can further take advantage of the first technique we developed in this work. Due to the block diagonal structure of the HTC-type Hamiltonian, one can decompose Chebyshev expansions for single and double excitation subspaces separately, and a shift in the energy axis of the subspace that significantly reduces the oscillation magnitude of the coefficients in time and allows a much larger propagation time step. These two theoretical approaches are general and can be applied to any trajectory-based non-adiabatic quantum dynamics methods.

Applying these two theoretical techniques, we extended the $\mathcal{L}$-PLDM method[80] to the collective coupling regime. Using this approach, we simulate the linear spectra of the N-molecule polaritonic system described by the HTC Hamiltonian. The approach we present here will significantly reduce computational costs. To demonstrate the developed methods, we simulate the polaritonic absorption spectra of $N = 500$ molecules coupled to a cavity under either static energy disorder or dipole orientation disorder, under which the permutation symmetry of the HTC Hamiltonian is broken and a simple mean-field approach is not directly applicable. We observe similar trends of these linear spectra as observed in the previous work.[74,75,81] As the disorder in energy σ_ε increases, the linewidth increases, and the Rabi splitting also gradually increases due to the disorders in energies. When gradually increasing the orientation disorder, the Rabi splitting decreases, without further change in the line width. In future work, we will outline the theoretical details of stimulating 2DES spectra for the polariton system under the collective coupling regime (Paper II), with new computational techniques for focusing the algorithm of the PLDM simulation.

ACKNOWLEDGMENTS

This work was supported by the Department of Energy under Grant No. DE-SC0022171. Computing resources were provided by the Center for Integrated Research Computing (CIRC) at the University of Rochester. The authors appreciate valuable discussions and comments from Ben Chng and Eric Koessler.

CONFLICT OF INTEREST

The authors have no conflicts of interest to disclose.

AVAILABILITY OF DATA

The data that support the findings of this work are available from the corresponding author on a reasonable request.

Appendix A: Cavity loss through Lindblad

The loss channel from state $|\mathrm{G}^1\rangle$ to state $|\mathrm{G}^0\rangle$ can be described by the loss operator

$$\hat{L} = |\mathrm{G}^0\rangle\langle\mathrm{G}^1|. \tag{A1}$$

The dissipator $\mathcal{L}_{\hat{L}}$ accounts for the cavity loss channel causing the system to relax

$$\mathcal{L}_{\hat{L}}[\hat{\rho}_\mathrm{Q}] = \Gamma\Big(\hat{L}\hat{\rho}_\mathrm{Q}\hat{L}^\dagger - \frac{1}{2}\{\hat{L}^\dagger\hat{L}, \hat{\rho}_\mathrm{Q}\}\Big), \tag{A2}$$

where Γ is the rate of relaxation of the jump operator which quantifies the coupling strength of the system to the environment, and $\{\hat{A}, \hat{B}\} = \hat{A}\hat{B} + \hat{B}\hat{A}$ is the anti-commutator, and $\hat{\rho}_\mathrm{Q} = \mathrm{Tr}_\mathrm{b}[\hat{\rho}]$ is the reduced density matrix operator for the quantum subsystem by tracing out all bath DOF. In this study, Γ is the cavity loss rate, and the cavity quality factor is defined as $\mathcal{Q} = \hbar\omega_\mathrm{c}/\Gamma$.

The Lindblad evolution for the forward and backward wavefunctions is computed by multiplying the forward and backward coefficients with a phase factor for these two states as

$$c_a(t + \mathrm{d}t) = \eta_a(t)c_a(t) \tag{A3}$$

$$\tilde{c}_a(t + \mathrm{d}t) = \tilde{\eta}_a(t)\tilde{c}_a(t) \tag{A4}$$

where the phase factors are

$$\eta_{\mathrm{G}^1} = \tilde{\eta}_{\mathrm{G}^1} = e^{-\Gamma\mathrm{d}t/2}, \tag{A5}$$

$$\eta_{\mathrm{G}^0} = \tilde{\eta}^*_{\mathrm{G}^0} = 1 + (2r-1)\sqrt{3(1-e^{-\Gamma\mathrm{d}t})\frac{c_{\mathrm{G}^1}(t)\tilde{c}^*_{\mathrm{G}^1}(t)}{c_{\mathrm{G}^0}(t)\tilde{c}^*_{\mathrm{G}^0}(t)}}, \tag{A6}$$

and $r \in [0,1]$ is a uniform random number. The phase factor, when averaged over the ensemble of trajectories ensures the exponential population decay of the state $|\mathrm{G}^1\rangle\langle\mathrm{G}^1|$ and a gain in population of the state $|\mathrm{G}^0\rangle\langle\mathrm{G}^0|$ as required by Lindblad dynamics, as analytically proved in our previous work[47,82]. The rest of the forward and backward coefficients, for $a \neq \mathrm{G}^1$ and $a \neq \mathrm{G}^0$ are not affected by the Lindblad decay, and the corresponding $\eta_a = \tilde{\eta}_a = 1$. When averaging among a reasonable amount of trajectories (typically $\sim 10^2$ trajectories, see Appendix B in Ref. 47), Eq. A5-A6 exactly reproduces the Lindblad EOM for reduced density matrix, as demonstrated numerically in our previous work.[47]

Appendix B: Error analysis for various propagators

We estimate the error accumulated during a propagation step Δt in the quantum subspace for various propagation schemes. We first compute the eigenstates of the HTC Hamiltonian and compute the exact propagator by

$$\exp\left(-\frac{i\hat{H}_{\mathrm{Q}}\Delta t}{\hbar}\right) = \hat{U}^{\dagger}\exp\left(-\frac{i\Delta t}{\hbar}\hat{\Lambda}\right)\hat{U} \tag{B1}$$

where $\hat{\Lambda}$ is the eigenvalues matrix (the diagonal form of $\hat{H}_{\mathrm{Q}}$), and $\hat{U}$ is the eigenvector matrix, satisfying $\hat{H}_{\mathrm{Q}}\hat{U} = \hat{\Lambda}\hat{U}$. The evolution of any vector can now be obtained by operating Eq. B1 on the vector. To test the accuracy of the different propagators, we generated $\mathcal{N} = 10^6$ samples of random state vectors by randomly selecting the coefficients in Eq. 26 (in the complex plane) while keeping it properly normalized. For each configuration, the bath fluctuation term $\sum_{\nu} C_{n,\nu}R_{n,\nu}$ in $\hat{H}_{\mathrm{Q}}$ (see Eq. 27) is also randomly sampled, based on the Wigner distribution (Eq. 72). For each value of the uncertainty parameter z, we compute the error of the propagator by comparing it against the exact evolution by

$$\text{error} = \frac{1}{\mathcal{N}}\sum_{\upsilon=1}^{\mathcal{N}} \max\left\{|c_i^{\upsilon} - c_i^{\mathrm{ex}}|\right\} \quad \forall i \in [1,\mathcal{K}] \tag{B2}$$

where c_i^{ex} are the components of the exactly propagated vector through Eq. B1 for υ_{th} trial and c_i^{υ} are the components of the vector propagated by the other numerical integrators.

In Fig. 8, we compare the accuracy of several propagators for one step propagation during Δt, as a function of the uncertainty parameter z (defined in Eq. 33). The red and orange curves present the standard symplectic integrator (using velocity-valet, Vel-Ver) and RK-4 propagators, respectively. For velocity verlet propagation, we further divided the integration into 1000 steps, with $\delta t = \Delta t/1000$. For RK-4, we use $\delta t = \Delta t/100$ and 100 steps for the Δt propagation. The light-cyan curve is the accuracy of the normal Chebyshev (Cheb) expansion without the separation of manifolds and the shift of the energy axis. We considered the first six terms of the Chebyshev expansion in Eq. 32 for the Δt propagation. For low z values up to $z \approx 0.25$, the quantum propagation via normal Chebyshev expansion for a single time step Δt is much more accurate compared to RK-4 or the velocity verlet. As we increase z, the accuracy of Chebyshev reduces and, around $z \approx 0.6$, it becomes worse than the velocity verlet propagation, due to the limited number of expansion terms (only six). Further increasing the number of terms will reduce the error. The dark-gray curve represents the Chebyshev propagator with the separate manifold and the shifting of the energy axis which we will refer to as the shifted Chebyshev (Shift-Cheb). As we separate the manifolds and shift the energy of the manifold, the accuracy of Chebyshev increases by orders of magnitude and it consistently performs much better than velocity verlet and RK-4 propagation even at a high value of z, with only six items used in the expansion.

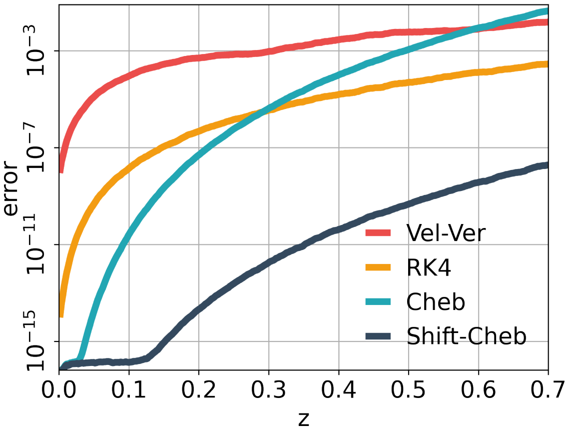

FIG. 8. Accuracy of different type propagators as a function of z-value (see Eq. 33). The red, yellow, cyan, and dark blue curves correspond to the symplectic integrator (velocity verlet), RK4, Chebyshev, and shifted Chebyshev propagators, respectively.

[1] F. Herrera and F. C. Spano, "Cavity-controlled chemistry in molecular ensembles," Phys. Rev. Lett. **116**, 238301 (2016).

[2] F. Herrera and F. C. Spano, "Theory of nanoscale organic cavities: The essential role of vibration-photon dressed states," ACS photonics **5**, 65–79 (2018).

[3] F. Herrera and F. C. Spano, "Absorption and photoluminescence in organic cavity qed," Phys. Rev. A: At. Mol. Opt. Phys. **95**, 053867 (2017).

[4] S. Takahashi and K. Watanabe, "Decoupling from a thermal bath via molecular polariton formation," J. Phys. Chem. Lett. **11**, 1349–1356 (2020).

[5] D. Xu, A. Mandal, J. M. Baxter, S.-W. Cheng, I. Lee, H. Su, S. Liu, D. R. Reichman, and M. Delor, "Ultrafast imaging of polariton propagation and interactions," Nature Communications **14**, 3881 (2023).

[6] R. Pandya, A. Ashoka, K. Georgiou, J. Sung, R. Jayaprakash, S. Renken, L. Gai, Z. Shen, A. Rao, and A. J. Musser, "Tuning the coherent propagation of organic exciton-polaritons through dark state delocalization," Advanced Science **9**, 2105569 (2022).

[7] M. Balasubrahmaniyam, A. Simkhovich, A. Golombek, G. Sandik, G. Ankonina, and T. Schwartz, "From enhanced dif-

fusion to ultrafast ballistic motion of hybrid light–matter excitations," Nature Materials **22**, 338–344 (2023).

[8] B. X. Chng, W. Ying, Y. Lai, A. N. Vamivakas, S. T. Cundiff, T. Krauss, and P. Huo, "Mechanism of polariton decoherence in the collective light-matter couplings regime," ChemRxiv (2024).

[9] E. O. Odewale, S. T. Wanasinghe, and A. S. Rury, "Assessing the determinants of cavity polariton relaxation using angle-resolved photoluminescence excitation spectroscopy," The Journal of Physical Chemistry Letters **15**, 5705–5713 (2024).

[10] C. A. DelPo, B. Kudisch, K. H. Park, S.-U.-Z. Khan, F. Fassioli, D. Fausti, B. P. Rand, and G. D. Scholes, "Polariton transitions in femtosecond transient absorption studies of ultrastrong light–molecule coupling," The journal of physical chemistry letters **11**, 2667–2674 (2020).

[11] T. M. Autry, G. Nardin, C. L. Smallwood, K. Silverman, D. Bajoni, A. Lemaître, S. Bouchoule, J. Bloch, and S. Cundiff, "Excitation ladder of cavity polaritons," Physical Review Letters **125**, 067403 (2020).

[12] M. Son, Z. T. Armstrong, R. T. Allen, A. Dhavamani, M. S. Arnold, and M. T. Zanni, "Energy cascades in donor-acceptor exciton-polaritons observed by ultrafast two-dimensional white-light spectroscopy," Nat. Commun. **13**, 7305 (2022).

[13] N. Peruffo, F. Mancin, and E. Collini, "Coherent dynamics in solutions of colloidal plexcitonic nanohybrids at room temperature," Advanced Optical Materials **11**, 2203010 (2023).

[14] L. Mewes, M. Wang, R. A. Ingle, K. Börjesson, and M. Chergui, "Energy relaxation pathways between light-matter states revealed by coherent two-dimensional spectroscopy," Communications Physics **3**, 157 (2020).

[15] T. Quenzel, D. Timmer, M. Gittinger, J. Zablocki, F. Zheng, M. Schiek, A. Lutzen, T. Frauenheim, S. Tretiak, M. Silies, *et al.*, "Plasmon-enhanced exciton delocalization in squaraine-type molecular aggregates," Acs Nano **16**, 4693–4704 (2022).

[16] M. Amin, E. R. Koessler, O. Morshed, F. Awan, N. M. Cogan, R. Collison, T. M. Tumiel, W. Girten, C. Leiter, A. N. Vamivakas, *et al.*, "Cavity controlled upconversion in cdse nanoplatelet polaritons," ACS nano (2024).

[17] O. Morshed, M. Amin, N. Cogan, E. R. Koessler, R. Collison, T. M. Tumiel, W. Girten, F. Awan, L. Mathis, P. Huo, *et al.*, "Room-temperature strong coupling between cdse nanoplatelets and a metal–dbr fabry–pérot cavity," The Journal of Chemical Physics **161** (2024).

[18] F. Freire-Fernández, N. G. Sinai, M. J. Hui Tan, S.-M. Park, E. R. Koessler, T. Krauss, P. Huo, and T. W. Odom, "Room-temperature polariton lasing from cdse core-only nanoplatelets," ACS nano (2024).

[19] L. Qiu, A. Mandal, O. Morshed, M. T. Meidenbauer, W. Girten, P. Huo, A. N. Vamivakas, and T. D. Krauss, "Molecular polaritons generated from strong coupling between cdse nanoplatelets and a dielectric optical cavity," The Journal of Physical Chemistry Letters **12**, 5030–5038 (2021).

[20] P. Fowler-Wright, B. W. Lovett, and v.-n. p. y. Jonathan Keeling, journal=Phys. Rev. Lett., "Efficient many-body non-markovian dynamics of organic polaritons," .

[21] L. P. Lindoy, A. Mandal, and D. R. Reichman, "Investigating the collective nature of cavity-modified chemical kinetics under vibrational strong coupling," Nanophotonics **13**, 2617–2633 (2024).

[22] J. B. Pérez-Sánchez, A. Koner, N. P. Stern, and J. Yuen-Zhou, "Simulating molecular polaritons in the collective regime using few-molecule models," Proceedings of the National Academy of Sciences **120**, e2219223120 (2023).

[23] J. B. Pérez-Sánchez, F. Mellini, J. Yuen-Zhou, and N. C. Giebink, "Collective polaritonic effects on chemical dynamics suppressed by disorder," Physical Review Research **6**, 013222 (2024).

[24] J. Del Pino, F. A. Schröder, A. W. Chin, J. Feist, and F. J. Garcia-Vidal, "Tensor network simulation of polaron-polaritons in organic microcavities," Physical Review B **98**, 165416 (2018).

[25] J. Provazza, F. Segatta, M. Garavelli, and D. F. Coker, "Semiclassical path integral calculation of nonlinear optical spectroscopy," J. Chem. Theory Comput. **14**, 856–866 (2018).

[26] P. Huo and D. F. Coker, "Communication: Partial linearized density matrix dynamics for dissipative, non-adiabatic quantum evolution," J. Chem. Phys. **135**, 201101 (2011).

[27] P. Huo and D. F. Coker, "Semi-classical path integral non-adiabatic dynamics: a partial linearized classical mapping hamiltonian approach," Mol. Phys. **110**, 1035–1052 (2012).

[28] M. K. Lee, P. Huo, and D. F. Coker, "Semiclassical path integral dynamics: Photosynthetic energy transfer with realistic environment interactions," Annu. Rev. Phys. Chem **67**, 639–668 (2016).

[29] H. L. Luk, J. Feist, J. J. Toppari, and G. Groenhof, "Multiscale molecular dynamics simulations of polaritonic chemistry," Journal of chemical theory and computation **13**, 4324–4335 (2017).

[30] R. H. Tichauer, D. Morozov, I. Sokolovskii, J. J. Toppari, and G. Groenhof, "Identifying vibrations that control non-adiabatic relaxation of polaritons in strongly coupled molecule–cavity systems," The Journal of Physical Chemistry Letters **13**, 6259–6267 (2022).

[31] G. Groenhof and J. J. Toppari, "Coherent light harvesting through strong coupling to confined light," The journal of physical chemistry letters **9**, 4848–4851 (2018).

[32] G. Groenhof, C. Climent, J. Feist, D. Morozov, and J. J. Toppari, "Tracking polariton relaxation with multiscale molecular dynamics simulations," The journal of physical chemistry letters **10**, 5476–5483 (2019).

[33] A. Dutta, V. Tiainen, I. Sokolovskii, L. Duarte, N. Markešević, D. Morozov, H. A. Qureshi, S. Pikker, G. Groenhof, and J. J. Toppari, "Thermal disorder prevents the suppression of ultrafast photochemistry in the strong light-matter coupling regime," Nature Communications **15**, 6600 (2024).

[34] I. Sokolovskii and G. Groenhof, "Photochemical initiation of polariton-mediated exciton propagation," Nanophotonics **13**, 2687–2694 (2024).

[35] M. Ben-Nun and T. J. Martınez, "Ab initio molecular dynamics study of cis–trans photoisomerization in ethylene," Chemical physics letters **298**, 57–65 (1998).

[36] B. Rana, E. G. Hohenstein, and T. J. Martínez, "Simulating the excited-state dynamics of polaritons with ab initio multiple," J. Phys. Chem. A. **128**, 139–151 (2024).

[37] R. Houdré, R. Stanley, and M. Ilegems, "Vacuum-field rabi splitting in the presence of inhomogeneous broadening: Resolution of a homogeneous linewidth in an inhomogeneously broadened system," Physical Review A **53**, 2711 (1996).

[38] Z. Zhou, H.-T. Chen, J. E. Subotnik, and A. Nitzan, "Interplay between disorder, local relaxation, and collective behavior for an ensemble of emitters outside versus inside a cavity," Physical Review A **108**, 023708 (2023).

[39] A. Mandal, M. A. Taylor, B. M. Weight, E. R. Koessler, X. Li, and P. Huo, "Theoretical advances in polariton chemistry and molecular cavity quantum electrodynamics," Chemical Reviews **123**, 9786–9879 (2023).

[40] P. L. Walters, T. C. Allen, and N. Makri, "Direct determination of discrete harmonic bath parameters from molecular dynamics simulations," J. Comput. Chem. **38**, 110–115 (2017).

[41] L. Valkunas, D. Abramavicius, and T. Mancal, *Molecular excitation dynamics and relaxation: quantum theory and spectroscopy* (John Wiley & Sons, 2013).

[42] E. Collini, "2d electronic spectroscopic techniques for quantum technology applications," J. Phys. Chem. C **125**, 13096–13108 (2021).

[43] A. M. Brańczyk, D. B. Turner, and G. D. Scholes, "Crossing disciplines-a view on two-dimensional optical spectroscopy," Ann. Phys. **526**, 31–49 (2014).

[44] P. Hamm and M. Zanni, *Concepts and Methods of 2D Infrared Spectroscopy* (Cambridge University Press, 2011).

[45] A. Gelzinis, R. Augulis, V. Butkus, B. Robert, and L. Valkunas, "Two-dimensional spectroscopy for non-specialists," Biochim. Biophys. Acta, Bioenerg. **1860**, 271–285 (2019).

[46] E. R. Koessler, A. Mandal, and P. Huo, "Incorporating lindblad decay dynamics into mixed quantum-classical simulations," J. Chem. Phys. **157**, 064101 (2022).

[47] M. E. Mondal, E. R. Koessler, J. Provazza, A. N. Vamivakas, S. T. Cundiff, T. D. Krauss, and P. Huo, "Quantum dynamics simulations of the 2d spectroscopy for exciton polaritons," The Journal of Chemical Physics **159** (2023).

[48] J. A. Campos-Gonzalez-Angulo, R. F. Ribeiro, and J. Yuen-Zhou, "Generalization of the tavis–cummings model for multi-level anharmonic systems," New Journal of Physics **23**, 063081 (2021).

[49] J. A. Campos-Gonzalez-Angulo and J. Yuen-Zhou, "Generalization of the tavis–cummings model for multi-level anharmonic systems: Insights on the second excitation manifold," The Journal of Chemical Physics **156** (2022).

[50] W. Ying, M. E. Mondal, and P. Huo, "Theory and quantum dynamics simulations of exciton-polariton motional narrowing," The Journal of Chemical Physics **161**, 064105 (2024).

[51] Y. Lai, W. Ying, and P. Huo, "Non-equilibrium rate theory for polariton relaxation dynamics," ChemRxiv (2024).

[52] P. Huo, T. F. Miller, and D. F. Coker, "Communication: Predictive partial linearized path integral simulation of condensed phase electron transfer dynamics," The Journal of Chemical Physics **139** (2013).

[53] P. Huo and D. F. Coker, "Consistent schemes for non-adiabatic dynamics derived from partial linearized density matrix propagation," J. Chem. Phys. **137**, 22A535 (2012).

[54] J. C. Tully, "Molecular dynamics with electronic transitions," The Journal of Chemical Physics **93**, 1061–1071 (1990).

[55] T. E. Li, B. Cui, J. E. Subotnik, and A. Nitzan, "Molecular polaritonics: Chemical dynamics under strong light–matter coupling," Annual review of physical chemistry **73**, 43–71 (2022).

[56] H.-D. Meyer and W. H. Miller, "A classical analog for electronic degrees of freedom in nonadiabatic collision processes," J. Chem. Phys. **70**, 3214–3223 (1979).

[57] J. R. Mannouch and J. O. Richardson, "A partially linearized spin-mapping approach for nonadiabatic dynamics. i. derivation of the theory," The Journal of chemical physics **153** (2020).

[58] J. R. Mannouch and J. O. Richardson, "A partially linearized spin-mapping approach for nonadiabatic dynamics. ii. analysis and comparison with related approaches," The Journal of chemical physics **153** (2020).

[59] D. Bossion, W. Ying, S. N. Chowdhury, and P. Huo, "Non-adiabatic mapping dynamics in the phase space of the su (n) lie group," The Journal of Chemical Physics **157** (2022).

[60] S. J. Cotton and W. H. Miller, "Symmetrical windowing for quantum states in quasi-classical trajectory simulations: Application to electronically non-adiabatic processes," The Journal of chemical physics **139** (2013).

[61] S. J. Cotton and W. H. Miller, "Symmetrical windowing for quantum states in quasi-classical trajectory simulations," The Journal of Physical Chemistry A **117**, 7190–7194 (2013).

[62] O. Walter, L. Cederbaum, and J. Schirmer, "The eigenvalue problem for "arrow"matrices," Journal of mathematical physics **25**, 729–737 (1984).

[63] D. P. O'Leary and G. W. Stewart, "Computing the eigenvalues and eigenvectors of symmetric arrowhead matrices," Journal of Computational Physics **90**, 497–505 (1990).

[64] N. J. Stor, I. Slapničar, and J. L. Barlow, "Accurate eigenvalue decomposition of real symmetric arrowhead matrices and applications," Linear algebra and its applications **464**, 62–89 (2015).

[65] S. K. Gray and D. E. Manolopoulos, "Symplectic integrators tailored to the time-dependent Schrödinger equation," The Journal of Chemical Physics **104**, 7099–7112 (1996).

[66] R. Kosloff, "Propagation methods for quantum molecular dynamics," Annual review of physical chemistry **45**, 145–178 (1994).

[67] M. Lee, P. Huo, and D. Coker, "Semi-classical path integral dynamics: Photosynthetic energy transfer with realistic environment interactions," Ann. Rev. Phys. Chem. **67**, 639 (2016).

[68] G. Stock and M. Thoss, "Semiclassical description of nonadiabatic quantum dynamics," Phys. Rev. Lett. **78**, 578 (1997).

[69] M. Thoss and G. Stock, "Mapping approach to the semiclassical description of nonadiabatic quantum dynamics," Phys Rev A **59**, 64 (1999).

[70] M. P. M. T. JO Richardson, P Meyer, "An analysis of nonadiabatic ring-polymer molecular dynamics and its application to vibronic spectra," Chem. Phys. **482**, 124–134 (2017).

[71] A. Kelly, R. van Zon, J. Schofield, and R. Kapral, "Mapping quantum-classical liouville equation: Projectors and trajectories," J. Chem. Phys **136**, 084101 (2012).

[72] M. S. Church, T. J. H. Hele, G. S. Ezra, and N. Ananth, "Nonadiabatic semiclassical dynamics in the mixed quantum-classical initial value representation," J. Comp. Phys. **148**, 102326 (2018).

[73] S. Takahashi and K. Watanabe, "Decoupling from a thermal bath via molecular polariton formation," J. Phys. Chem. Lett. **11**, 1349–1356 (2020).

[74] K. Schwennicke and J. Y.-Z. N.C. Giebink, "Extracting accurate light-matter couplings from disordered polaritons," Nanophotonics **13** (2024).

[75] G. Engelhardt and J. Cao, "Unusual dynamical properties of disordered polaritons in microcavities," Phys. Rev. B. **105**, 064205 (2022).

[76] J. Yuen-Zhou and A. Koner, "Linear response of molecular polaritons," The Journal of Chemical Physics **160** (2024).

[77] S. T. Wanasinghe, A. Gjoni, W. Burson, C. Majeski, B. Zaslona, and A. S. Rury, "Motional narrowing through photonic exchange: Rational suppression of excitonic disorder from molecular cavity polariton formation," J. Phys. Chem. Lett. **15**, 2405–2418 (2024).

[78] E. O. Odewale, S. T. Wanasinghe, and A. S. Rury, "Assessing the determinants of cavity polariton relaxation using angle-resolved photoluminescence excitation spectroscopy," J. Phys. Chem. Lett. **15**, 5705–5713 (2024).

[79] S. Mukamel, *Principles of Nonlinear Optical Spectroscopy* (Oxford University Press, 1995).

[80] S. Mondal and S. Keshavamurthy, "Phase space perspective on a model for isomerization in an optical cavity," J. Chem. Phys. **159**, 074106 (2023).

[81] H.-T. Chen, Z. Zhou, M. Sukharev, J. E. Subotnik, and A. Nitzan, "Interplay between disorder and collective coherent response: Superradiance and spectral motional narrowing in the time domain," Phys. Rev. A. **106**, 053703 (2022).

[82] E. R. Koessler, A. Mandal, and P. Huo, "Incorporating lindblad decay dynamics into mixed quantum-classical simulations," J. Chem. Phys. **157**, 064101 (2022).